

Precipitation Processes and Vortex Alignment during the Intensification of a Weak Tropical Cyclone in Moderate Vertical Shear

ROBERT F. ROGERS AND PAUL D. REASOR

NOAA/Atlantic Oceanographic and Meteorological Laboratory/Hurricane Research Division, Miami, Florida

JONATHAN A. ZAWISLAK

NOAA/Atlantic Oceanographic and Meteorological Laboratory/Hurricane Research Division, and Cooperative Institute for Marine and Atmospheric Studies, Rosenstiel School of Marine and Atmospheric Science, Miami, Florida

LEON T. NGUYEN

Oregon State University, Corvallis, Oregon

(Manuscript received 25 September 2019, in final form 8 January 2020)

ABSTRACT

The mechanisms underlying the development of a deep, aligned vortex, and the role of convection and vertical shear in this process, are explored by examining airborne Doppler radar and deep-layer dropsonde observations of the intensification of Hurricane Hermine (2016), a long-lived tropical depression that intensified to hurricane strength in the presence of moderate vertical wind shear. During Hermine's intensification the low-level circulation appeared to shift toward locations of deep convection that occurred primarily downshear. Hermine began to steadily intensify once a compact low-level vortex developed within a region of deep convection in close proximity to a midlevel circulation, causing vorticity to amplify in the lower troposphere primarily through stretching and tilting from the deep convection. A notable transition of the vertical mass flux profile downshear of the low-level vortex to a bottom-heavy profile also occurred at this time. The transition in the mass flux profile was associated with more widespread moderate convection and a change in the structure of the deep convection to a bottom-heavy mass flux profile, resulting in greater stretching of vorticity in the lower troposphere of the downshear environment. These structural changes in the convection were related to a moistening in the midtroposphere downshear, a stabilization in the lower troposphere, and the development of a mid- to upper-level warm anomaly associated with the developing midlevel circulation. The evolution of precipitation structure shown here suggests a multiscale cooperative interaction across the convective and mesoscale that facilitates an aligned vortex that persists beyond convective time scales, allowing Hermine to steadily intensify to hurricane strength.

1. Introduction

A key factor for tropical cyclone (TC) intensification is the presence of symmetry within the TC inner core. Early theories of TC intensification are based on an axisymmetric view of TCs where there is a feedback among surface fluxes, near-surface convergence of angular momentum, and latent heat release (Ooyama 1964, 1969, 1982; Charney and Eliassen 1964). A more recent rotating convection paradigm for TC intensification accounts for the commonly observed asymmetric distribution of convection, especially during the early

stages of intensification. It highlights the role of aggregation, merger and axisymmetrization of convectively generated vorticity during the intensification process (Nguyen et al. 2008; Montgomery and Smith 2014). Although the intensification mechanism involving localized, rotating convection is fundamentally three-dimensional and asymmetric, the evolution of axisymmetric tangential wind can still be usefully viewed in terms of the conventional axisymmetric view extended to include eddy fluxes of heat and momentum and unbalanced boundary layer processes (e.g., Smith et al. 2009). The development of a deep, vertically aligned vortex, either through the reduction of tilt or the development of a vortex above (below) an

Corresponding author: Robert Rogers, robert.rogers@noaa.gov

DOI: 10.1175/MWR-D-19-0315.1

© 2020 American Meteorological Society. For information regarding reuse of this content and general copyright information, consult the [AMS Copyright Policy](https://www.ametsoc.org/PUBSReuseLicenses) (www.ametsoc.org/PUBSReuseLicenses).

existing low-level (midlevel) circulation center, facilitates symmetry and is thus a critical step in the intensification process (Dunkerton et al. 2009; Wang et al. 2012; Munsell et al. 2017; Rios-Berrios et al. 2018; Ryglicki et al. 2018; Miyamoto and Nolan 2018; Chen et al. 2018; Alvey et al. 2020). This consideration is relevant for TCs at all stages in their early life cycle: from predepression up through tropical storm strength.

Precipitation processes play an important role in intensification. One line of research related to the rotating convection paradigm focuses on deep convective towers, termed vortical hot towers (VHTs), which collectively drive a system-scale inflow during the genesis process (Hendricks et al. 2004; Montgomery et al. 2006; Nguyen et al. 2008; Montgomery and Smith 2014). This idea was broadened in Dunkerton et al. (2009), who proposed the “marsupial paradigm” that provides a theoretical framework for understanding tropical cyclogenesis in easterly waves. The Kelvin cat’s eye within the critical layer, or “wave pouch,” was identified as a favorable environment for tropical cyclogenesis. The quasi-closed circulation in this comoving frame of reference favors persistent deep convection, vorticity aggregation, and moistening, increasing the likelihood of genesis (Montgomery et al. 2010; Wang et al. 2010a,b; Wang 2012). Houze et al. (2009) noted the importance of an intense convective cell in stretching lower-tropospheric vorticity during the development of the system that became Hurricane Ophelia (2005). Bell and Montgomery (2010) analyzed airborne Doppler measurements of an area of deep convection in predepression Hagupit in the western Pacific, and found that the low-level circulation of the pre-depression disturbance was enhanced by the coupling of the low-level vorticity and convergence in the deep convection, consistent with Dunkerton, Montgomery, and Wang’s work.

Other studies approach the development of a deep, aligned vortex and subsequent intensification from a more mesoscale perspective, focusing on the local thermodynamic environment and its impact on the vertical mass flux profile within a mesoscale domain. Raymond et al. (2011), Raymond and López Carrillo (2011), and Gjorgjievska and Raymond (2014) note that a midlevel vortex is more conducive for convection with a vertical mass flux profile that peaks in the lower troposphere—what they term a “bottom-heavy” mass flux profile—which is associated with strong low-level convergence of mass and vorticity and a spinup of the low-level cyclone. While the Houze et al. (2009) Ophelia study focused on an intense convective cell, they noted that the mass flux profile in the lower troposphere within the convective cell peaked in the

lower troposphere, resulting in a maximum in potential vorticity production in that layer.

Both of the approaches mentioned above presume a specific structure to the precipitation within the mesoscale environment of the low- and midlevel circulation centers. The structure of the precipitation (e.g., convective or stratiform; deep, moderate, or shallow convection) determines parameters such as the profiles of vertical velocity, vertical mass flux, and divergence, which has important implications for vorticity production. The precipitation structure can also be modulated by environmental conditions such as humidity and static stability. For example, idealized modeling by Kilroy and Smith (2012) showed that low- to midlevel dry air weakens updrafts and downdrafts in tropical cyclogenesis environments, consistent with similar work by James and Markowski (2010) in midlatitude environments. James and Markowski (2010) did find, however, that the weakening effect of dry air on updrafts is reduced in cases of high instability. For low instability, though, a humid environment is required for convection to sustain itself and grow. In an examination of deep-layer dropsondes from a variety of field campaigns in the Atlantic and Pacific basins, Raymond et al. (2014) noted that thermodynamic profiles with a lower instability index were associated with midlevel vortices, more humid environments, and more bottom-heavy mass flux profiles. Such profiles were more likely to develop into tropical storms within 48 h. Bell and Montgomery (2019), by contrast, argued that cycles of deep convection and stratiform precipitation in Hurricane Karl (2010), tied to the diurnal cycle, alternately build the low- and midlevel circulations episodically, rather than through a sustained lowering of the convective mass flux associated with stabilization as suggested by Raymond et al. (2014).

Vertical shear complicates the symmetrization process, as it forces a wavenumber-1 asymmetry in the kinematic, thermodynamic, and precipitation fields (Jones 1995; Heymsfield et al. 2001; Reasor et al. 2013, among many others). Vertical shear has also been shown to limit TC intensification through midlevel ventilation of dry air (Riehl and Malkus 1961; Emanuel et al. 2004; Tang and Emanuel 2010) and flushing and stabilization of the boundary layer in downdrafts (Riemer et al. 2010). Shear also leads to a misalignment between low- and midlevel circulations, resulting in strong relative flow over a low-level circulation center, making the overall system vulnerable to any dry air that exists nearby and limiting the chances of development (Davis and Ahijevych 2012).

While shear typically limits TC intensification, there are some situations where intensification can occur

despite the presence of shear, particularly when the shear is of moderate strength (broadly defined as 850–200-hPa shear magnitudes ranging between 5 and 10 m s^{-1}). This intensification can occur when there is forcing of strong convection downshear providing a significant projection onto wavenumber-0 (Reasor et al. 2009; Nguyen and Molinari 2012), when precipitation and deep convection occur and persist on the upshear side (Jiang 2012; Stevenson et al. 2014; Alvey et al. 2015; Rogers et al. 2015, 2016; Susca-Lopata et al. 2015; Tao and Zhang 2015; Zawislak et al. 2016; Nguyen et al. 2017; Munsell et al. 2017; Wadler et al. 2018; Leighton et al. 2018; Rios-Berrios et al. 2018), and through downshear reformation (Molinari et al. 2004, 2006; Molinari and Vollaro 2010; Nguyen and Molinari 2015; Chen et al. 2018). The uncertain impacts of these processes in moderate shear is manifested as a pronounced forecasting challenge (Bhatia and Nolan 2013; Tao and Zhang 2015; Finocchio and Majumdar 2017), and this has been identified as a key challenge by the National Hurricane Center (NTSB 2017).

With these uncertainties in mind, a series of aircraft missions into Hurricane Hermine (2016), a TC that developed in the eastern Gulf of Mexico in late August, is analyzed here. Hermine was a long-lived tropical depression that eventually intensified into a tropical storm and then a hurricane in the presence of persistent moderate vertical shear before making landfall in the Florida Panhandle. The kinematic and thermodynamic structure and evolution of Hermine will be examined here to address the following questions related to the intensification of weak TCs in moderate shear:

- 1) What was the evolution of the low- and midlevel circulations during Hermine's development?
- 2) How did the structure of precipitation evolve and what was the impact of this evolution on the development of Hermine?
- 3) What role did vertical shear play in Hermine's development?

These questions will be addressed by an analysis of data collected by a variety of aircraft that sampled Hermine for much of its life cycle.

2. Methodology

a. Description of case

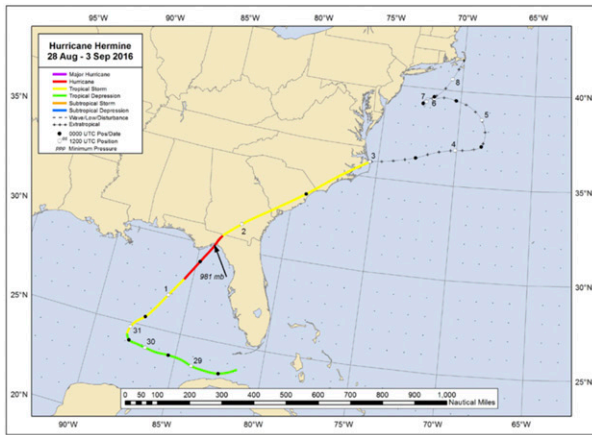
Hermine developed from a tropical wave that emerged off Africa on 17 August 2016. As the wave moved across the Atlantic it encountered conditions hostile to genesis, including vertical wind shear and dry midlevel air from an upper-level trough that inhibited sustained deep convection (Berg 2016). Once the wave reached

the Florida Straits, though, its forward motion slowed significantly and it was declared Tropical Depression 9 (TD-9) at 1800 UTC 28 August. TD-9 tracked toward the west-northwest, just north of the coast of Cuba (Fig. 1), for about three days. The forward motion continued to slow, and by 31 August TD-9 turned toward the northeast and intensified to Tropical Storm Hermine. Steady strengthening ensued as Hermine accelerated its forward motion and intensified to hurricane strength just prior to landfall at 0530 UTC 2 September in the Florida Panhandle.

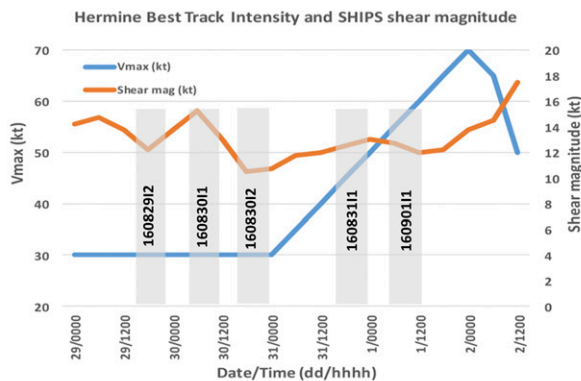
Time series of 850–200-hPa shear magnitude and heading from the Statistical Hurricane Intensity Prediction Scheme (SHIPS; DeMaria and Kaplan 1999) analyses are shown in Figs. 1b and 1c. The shear magnitude (Fig. 1b) stays within the moderate range (between 10–20 kt, or $\sim 5\text{--}10 \text{ m s}^{-1}$) for the entire time considered here. This includes while Hermine was a long-lived tropical depression and when it steadily intensified to a hurricane. The shear heading (Fig. 1c) shows that shear was primarily toward the east and southeast (i.e., from the west and northwest), except near landfall, when the shear turned to be more toward the northeast (i.e., from the southwest). The shear pattern was associated with a weak upper-level low in the western Gulf of Mexico coupled with southeasterly flow at 850 hPa as Hermine was positioned at the southwestern portion of a large subtropical anticyclone in the western Atlantic (not shown). This general westerly to northwesterly shear pattern remained in place for most of the time Hermine was a tropical depression and during its early intensification period toward hurricane status.

The midlevel relative humidity (defined here as the 700–400-hPa layer mean) during the morning of 30 August (Fig. 2a) showed high moisture to the south and east and a localized area of dry air over the southern Gulf states and into the northern Gulf, north of TD-9. Figures 2c and 2d show the midlevel relative humidity from all dropsondes released by the high-altitude NASA Global Hawk aircraft within 500 km of the estimated midlevel center when the Global Hawk was in the storm environment. The humidity pattern shown in Fig. 2a was reflected in the Global Hawk dropsonde measurements (Fig. 2c). The humidity field showed a similar asymmetry two days later when Hermine was approaching hurricane status near the Florida coast (Fig. 2b), with a distinct west–east gradient in humidity across the storm and its near environment to the north. Global Hawk dropsondes during this period (Fig. 2d) again depicted this humidity gradient.

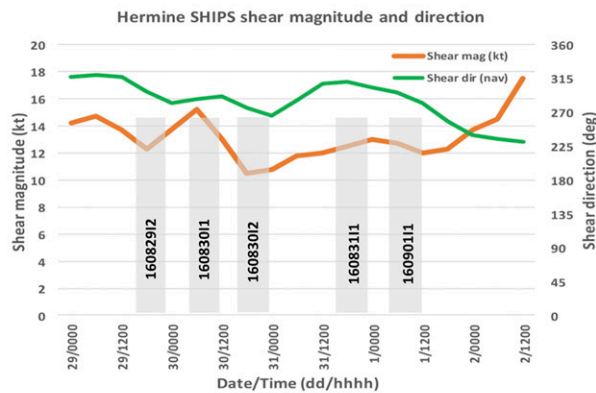
Infrared satellite imagery (Fig. 3) showed that Hermine consisted of disorganized areas of cold cloud tops early in its



(a)



(b)



(c)

FIG. 1. (a) Position and intensity of Hermine (2016) from NHC best track (image courtesy www.nhc.noaa.gov). (b) Time series of best track intensity (kt; blue line) and 850–200-hPa SHIPS shear (kt; orange line). Gray bars denote approximate times of WP-3D missions and mission ID. (c) As in (b), but green line denotes 850–200-hPa SHIPS direction (navigational degrees; 180° = shear from the south; 270° = shear from the west, etc.).

life cycle. As Hermine slowed its forward motion and began its turn toward the northeast there was a broader shield of cold cloud tops (Fig. 3b), though the displacement of the cloud shield to the southeast of the location of the NHC best track was indicative of the west-northwesterly shear impacting the system. Cold cloud cirrus canopies were transient and intermittent for ~36–48 h (not shown). Once Hermine became a tropical storm, a more persistent cold cloud shield developed (Fig. 3d), though the shield exhibited an elongated structure, with isolated areas of cloud top temperatures < -80°C located generally to the south of the low-level center and a lack of cold cloud top temperatures to the north and west. This cloud structure was consistent with the asymmetries in the humidity environment shown in Fig. 2. The final satellite image shown, as Hermine was approaching hurricane strength (Fig. 3e), showed a more extensive, concentrated region of cloud top temperatures < -80°C. Even then, though, most of the coldest cloud tops were located on the southeast side of the storm, indicative of the westerly component of moderate shear still impacting the system (cf. Fig. 1).

b. Description of data

Hermine was well sampled by a variety of aircraft during most of its life cycle, including NOAA WP-3D (hereafter P-3) and G-IV aircraft, as a part of the NOAA Intensity Forecasting Experiment (IFEX; Rogers et al. 2006, 2013), and the NASA Global Hawk (hereafter GH) as a part of the NOAA Sensing Hazards with Operational Unmanned Technology (SHOUT; Wick et al. 2020) campaign. These aircraft provided flight-level, dropsonde, and airborne Doppler radar observations of Hermine’s structure and evolution. This included full-tropospheric dropsonde profiles from the Global Hawk for two of the days considered here. The P-3 missions occurred at ~12 h frequency (cf. Fig. 1), including for the extended period that Hermine was classified as a tropical depression up through hurricane strength. These missions occurred both while Hermine was tracking west-northwest in the southeast Gulf of Mexico and after it had completed its turn toward the north-northeast. The flight patterns flown during the P-3 missions consisted of a series of radial legs oriented at different azimuths around the storm. Since most of these missions were reconnaissance missions tasked by the National Hurricane Center, the flight altitudes were ~1.5 km. The only temporal gap in coverage was ~12–18 h after when Hermine was first classified as a tropical storm in the best track (cf. Fig. 1). Table 1 provides the on-station times for the five P-3 missions considered here.

Key observations provided by the P-3 analyzed here include airborne tail-Doppler radar (hereafter TDR)

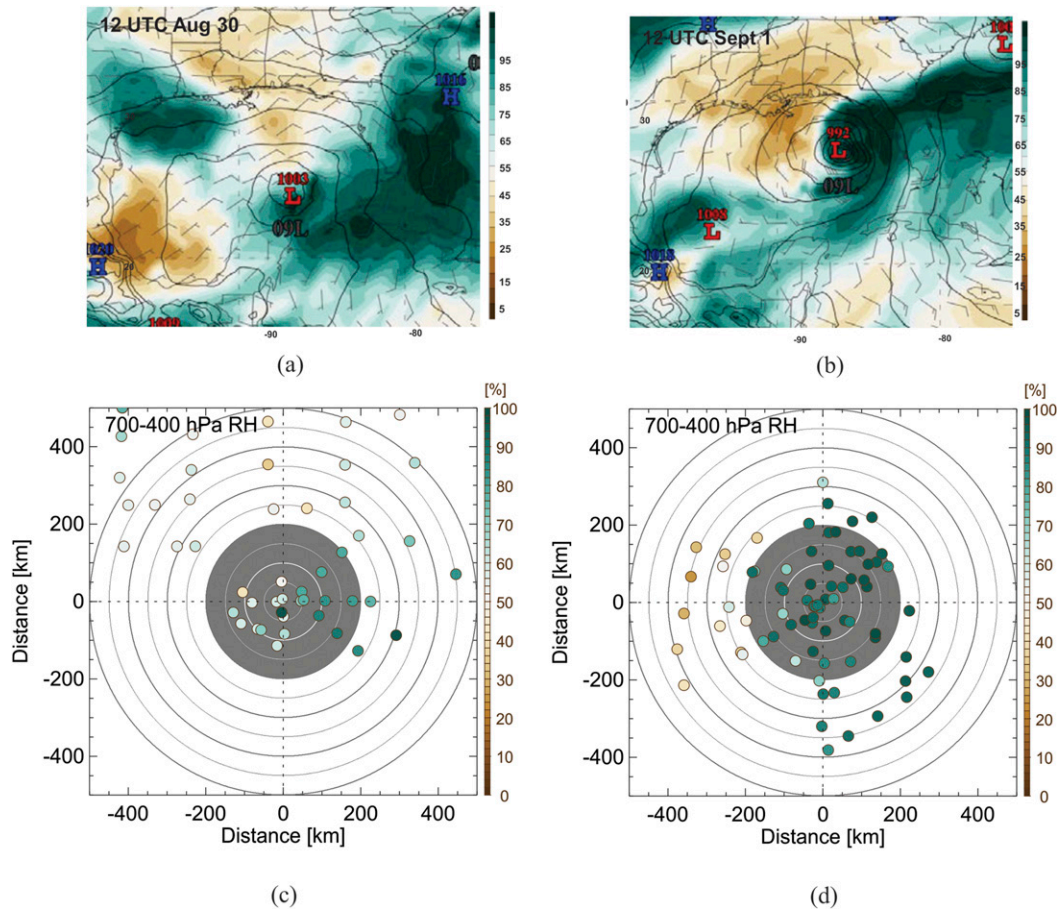


FIG. 2. (a) Global Forecast System (GFS) analysis of 700–400-hPa relative humidity (shaded, percent) and mean sea level pressure (contour, hPa) valid 1200 UTC 30 Aug. (b) As in (a), but for 1200 UTC 1 Sep. (c) Locations of dropsondes from NASA Global Hawk mission during 30 Aug. Shading denotes layer-averaged 700–400-hPa relative humidity (%) from the dropsondes. Gray circle denotes 200-km radius region centered on the approximate midlevel center. (d) As in (c), but for 1 Sep Global Hawk mission.

observations of winds and reflectivity and dropsonde measurements providing near-vertical profiles of temperature, moisture, wind, and pressure below flight level. Three-dimensional analyses of winds and reflectivity from the TDR are created for each radial pass through the flight-level center using the variational algorithm as described in Gamache (1997) and used in Rogers et al. (2012) and Reasor et al. (2013), and many other papers. Individual radial passes, separated by an average of ~ 80 min, are used to assess vortex- and convective-scale structure and its variability at a relatively high temporal resolution. More slowly evolving vortex-scale fields (e.g., azimuthally averaged structures) are assessed using analyses where the individual radial passes are merged together (termed “merged analyses” here) to yield a composite view of TC structure, with greater spatial coverage, and covering typically a ~ 4 h time

window. A similar analysis methodology was employed in Rogers et al. (2015, 2016).

The GH flew two missions, each lasting ~ 23 – 24 h, on 29–30 August and 31 August–1 September. Both missions operated out of the GH base in Wallops Island, Virginia, and included dropsondes off the southeast coast of the United States as well as over Hermine in the Gulf of Mexico (cf. Fig. 2). The GH reached altitudes of ~ 18 km, allowing for dropsonde profiles that cover the entire troposphere and lower stratosphere. Table 2 provides the approximate on-station times for the two GH missions shown here.

3. Results

a. Kinematic structure and evolution

Figure 4 shows storm-relative flow using merged Doppler analyses from each of the five P-3 Hermine

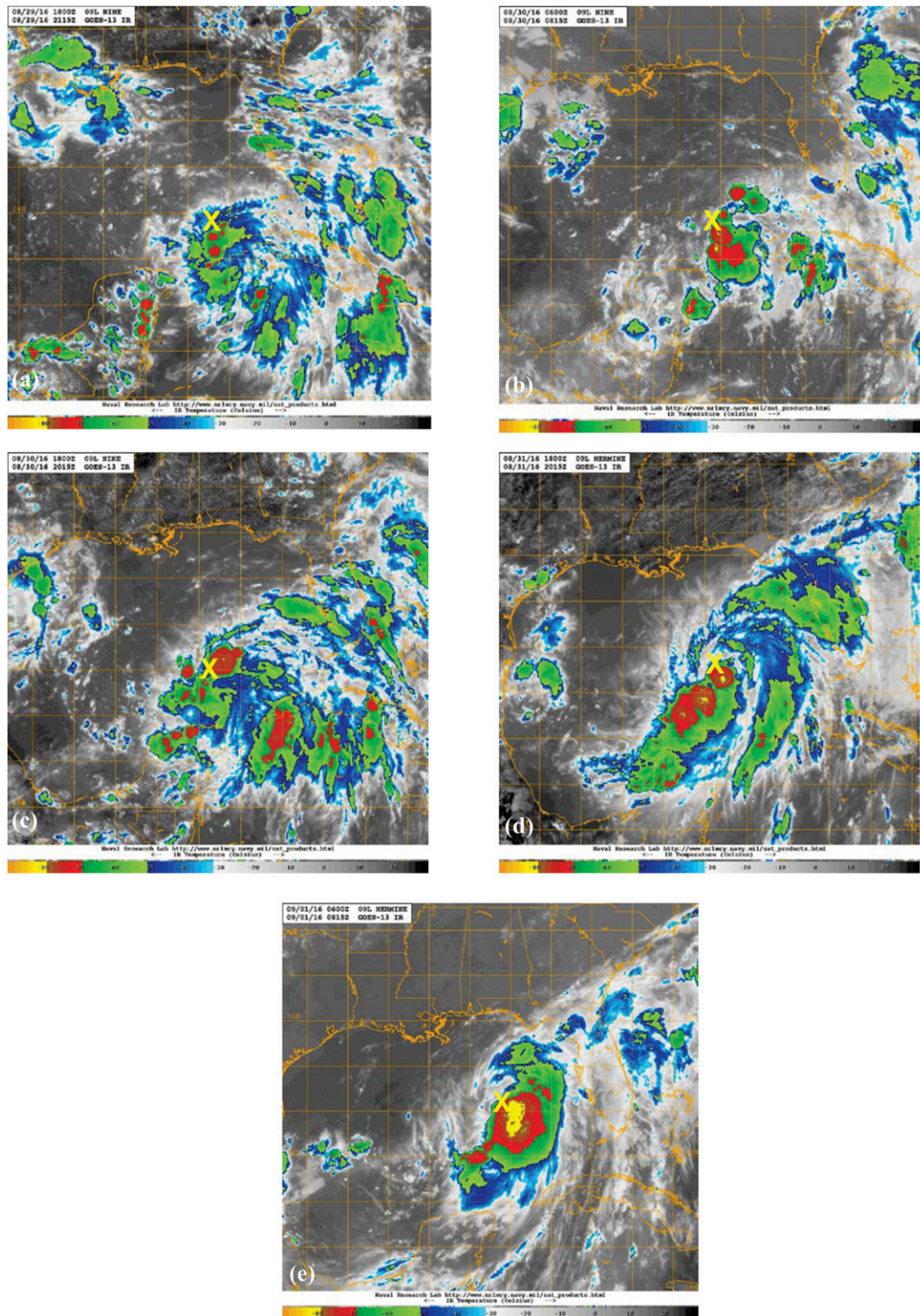


FIG. 3. *GOES-13* enhanced infrared imagery valid (a) 2115 UTC 29 Aug, (b) 0815 UTC 30 Aug, (c) 2015 UTC 30 Aug, (d) 2015 UTC 31 Aug, and (e) 0815 UTC 1 Sep. Images courtesy www.nrlmyr.navy.mil. Yellow “X” in each panel denotes location of NHC best track.

TABLE 1. Mission numbers, identifications, time of first and last center passes (UTC), and nearest 6-h best track intensity for five P-3 missions shown here.

Mission number	Mission ID	Time of first center pass (UTC)	Time of last center pass (UTC)	Nearest 6-h best track intensity (kt)
1	160829I2	1946	2247	30
2	160830I1	0553	0957	30
3	160830I2	1756	2303	30
4	160831I1	1742	2310	45
5	160901I1	0539	1103	55

missions at 2- and 5-km altitude, along with wind speed at 2 km and the 850–200-hPa shear vector as defined by SHIPS. Storm motion for each time period was estimated from the NHC best track positions. The low-level (2-km) circulation was clearly defined for all of the missions shown here. During the first three missions, when Hermine was a tropical depression, the midlevel (5-km) circulation, however, was less well-defined—sometimes appearing as a diffuse circulation comprised of multiple centers (cf. Fig. 4b) and sometimes practically undetectable within the domain shown here (cf. Fig. 4c)—and showed a clear displacement from the low-level circulation. The magnitude of the displacement was ~100–150 km from the low-level (i.e., 2-km) circulation during these early missions, and the direction of the displacement was generally to the south and southeast of the low-level circulation (i.e., on the downshear side of the storm). Peak low-level winds during the depression stage were ~10–15 m s^{-1} . For the mission after when Hermine was declared a tropical storm (i.e., mission 160831I1, Fig. 4d) a notable transition in the structure of the vortex had occurred. The midlevel circulation center was much closer (~25 km) to the low-level circulation, and the low-level wind speeds had increased to 15–20 m s^{-1} in locations mostly southeast (downshear) of the low-level center. The subsequent mission (Fig. 4e) showed that Hermine continued its intensification, as the upper-level circulation was now displaced only ~10 km downshear from the low-level circulation and peak winds in excess of 25 m s^{-1} covered a broad region on the southeast side of the storm. The displacement of the midlevel circulation was well within the low-level RMW of ~75 km, indicating the vortex was essentially aligned through that layer.

Figure 5 shows the azimuthally averaged tangential wind for each mission. Center positions used to construct these analyses were taken from real-time flight-level winds, which seek to locate the minimum wind speed at flight level (~1.5 km for these missions) and determine the center from those measurements

following Willoughby and Chelmon (1982). These flight-level centers represent the best estimate of the storm center, as radar-based center-finding algorithms are deficient in this case because of insufficient data coverage from a lack of scatterers and a lack of organization required for more sophisticated algorithms (e.g., calculating vorticity centroids or maximizing tangential wind in an annulus surrounding the RMW) (Marks et al. 1992; Reasor et al. 2009; Reasor and Eastin 2012). The azimuthally averaged tangential wind field shown in Fig. 5 largely reflected the evolution shown in Fig. 4, as the first three missions showed a shallow vortex confined below ~4–5-km altitude. The presence of a shallow vortex during the earlier missions was an indication either of a misalignment between the low- and midlevel circulations, similar to that seen in Hurricane Earl (2010) at a similar stage of its life cycle (Rogers et al. 2015), or the absence of a midlevel circulation. Once Hermine was declared a tropical storm and was intensifying (i.e., mission 160831I1), the depth of the cyclonic circulation grew to extend over most of the troposphere. It should be noted, though, that there was considerable structural evolution that occurred during this mission (discussed below), and the center estimates during the first two passes that comprised this mission were less certain. As a result, caution should be exercised in interpreting the azimuthal-mean field during mission 160831I1. This caution is reflected by the apparent double peak structure seen in the azimuthal-mean tangential wind field; that is, one peak at ~50 km and the other at ~150 km

TABLE 2. Mission numbers, identifications, and approximate start and end times when the GH was in the storm environment of Hermine.

Mission number	Starting date/time in storm environment	Ending date/time in storm environment
GH1	0530 UTC 29 Aug	1630 UTC 29 Aug
GH2	0700 UTC 1 Sep	1800 UTC 1 Sep

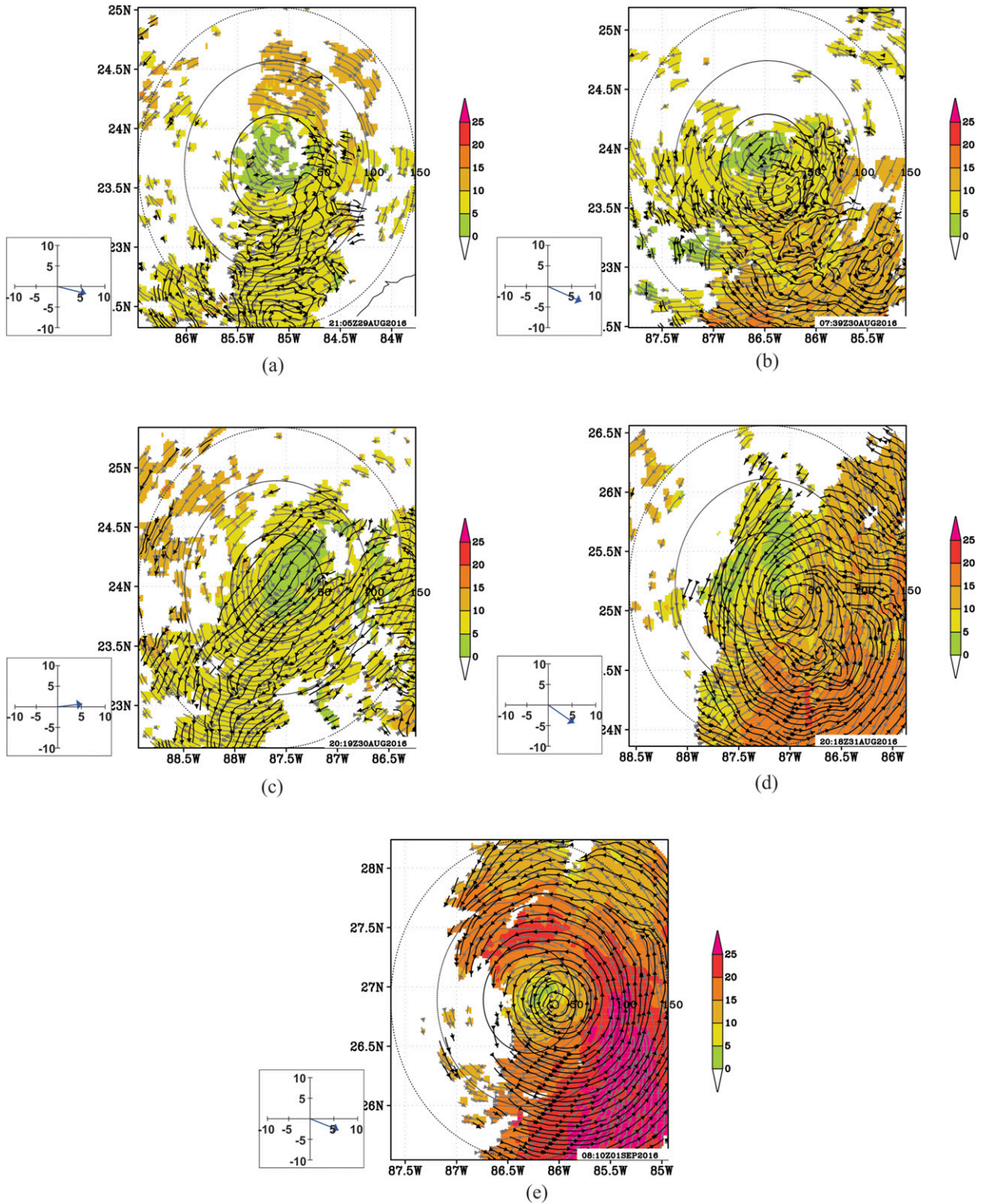


FIG. 4. Storm-relative streamlines at 2-km (gray) and 5-km (black) altitude and storm-relative wind speed (shaded, m s^{-1}) at 2-km altitude from merged P-3 Doppler analyses for missions (a) 160829I2, (b) 160830I1, (c) 160830I2, (d) 160831I1, and (e) 160901I1. Range rings (km) from the 2-km center indicated by circles. Box in lower-left corner of each panel denotes 850–200-hPa SHIPS shear vector (m s^{-1}) for the nearest 6-h time to the center time of the analysis given in lower-right corner.

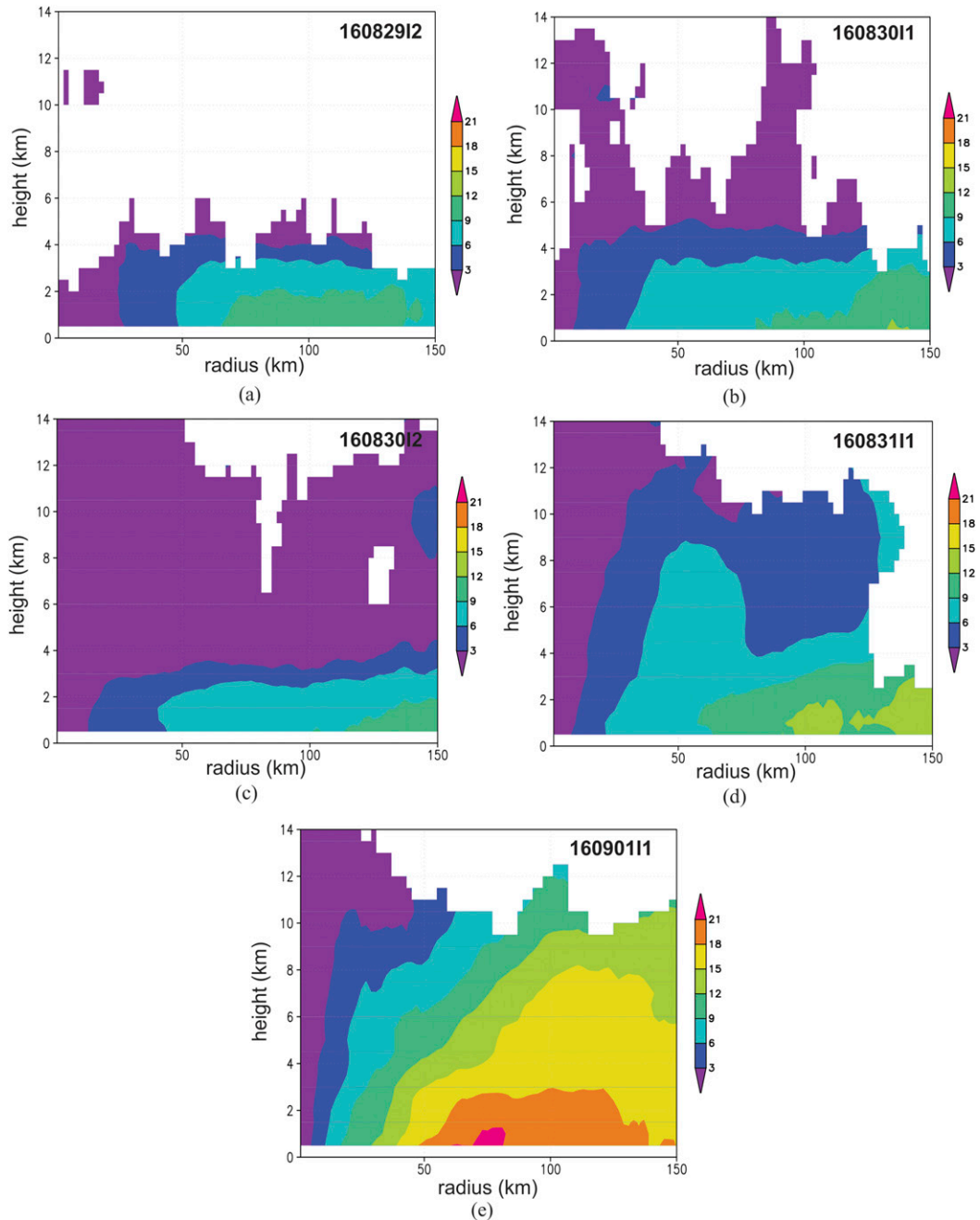


FIG. 5. Radius–height plot of azimuthally averaged tangential winds (shaded, m s^{-1}). Azimuthal averages require at least 50% of contiguous coverage in azimuth at any point in radius–height space to be calculated.

radius, seen in Fig. 5d. By the time of the final mission, though, Hermine’s azimuthal-mean wind was well-defined, exhibiting an outward-sloping azimuthally averaged tangential wind structure with peak low-level values $> 20 \text{ m s}^{-1}$ located at ~ 75 -km radius.

Because of the ~ 20 h separation in time between the 160830I2 and 160831I1 missions (cf. Table 1), a

detailed evolution of the vortex alignment cannot be determined between these missions. However, examining individual radial passes, each separated by ~ 75 min during the ~ 5.5 h that the P-3 was on station in 160831I1, provides the opportunity to examine the evolution of the low- and midlevel circulations on these time scales during the mission. Figure 6 shows storm-relative flow fields at 2 and 5 km as well as the

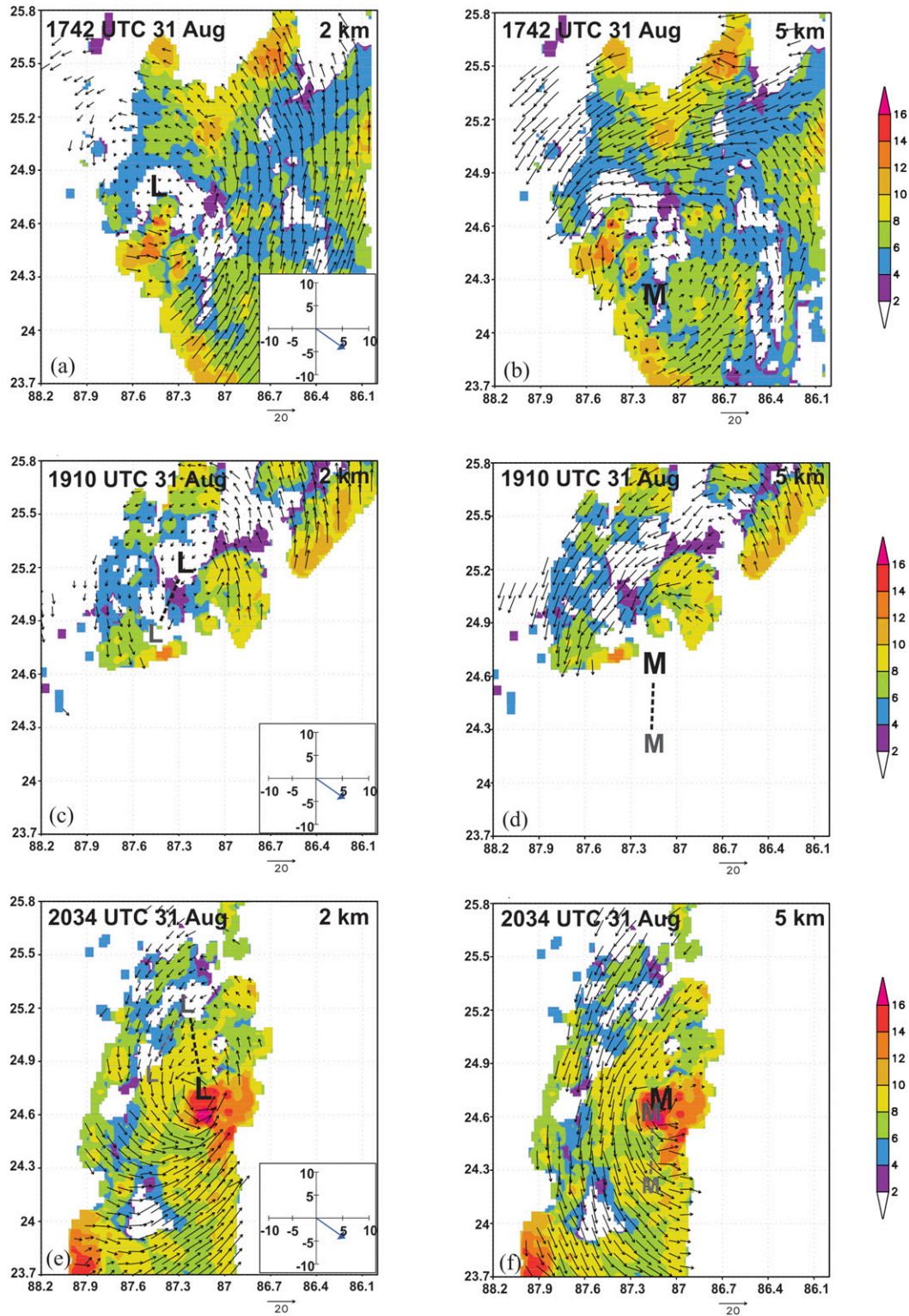


FIG. 6a. (a) 20 dBZ echo top heights (shaded, km) and storm-relative winds (vectors, m s^{-1}) at 2-km altitude for individual radial passes centered at 1742 UTC 31 Aug; (b) as in (a), but for winds at 5-km altitude; (c) as in (a), but for 1910 UTC 31 Aug; (d) as in (b), but for 1910 UTC 31 Aug; (e) as in (a), but for 2034 UTC 31 Aug; and (f) as in (b), but for 2034 UTC 31 Aug. “L” and “M” denote locations of subjectively determined circulation centers at 2- and 5-km altitudes, respectively. Lighter, smaller letters denote locations from previous radial passes. Inset in lower right corner in (a),(c),(e) denotes SHIPS-derived 850–200-hPa shear, as in Fig. 4.

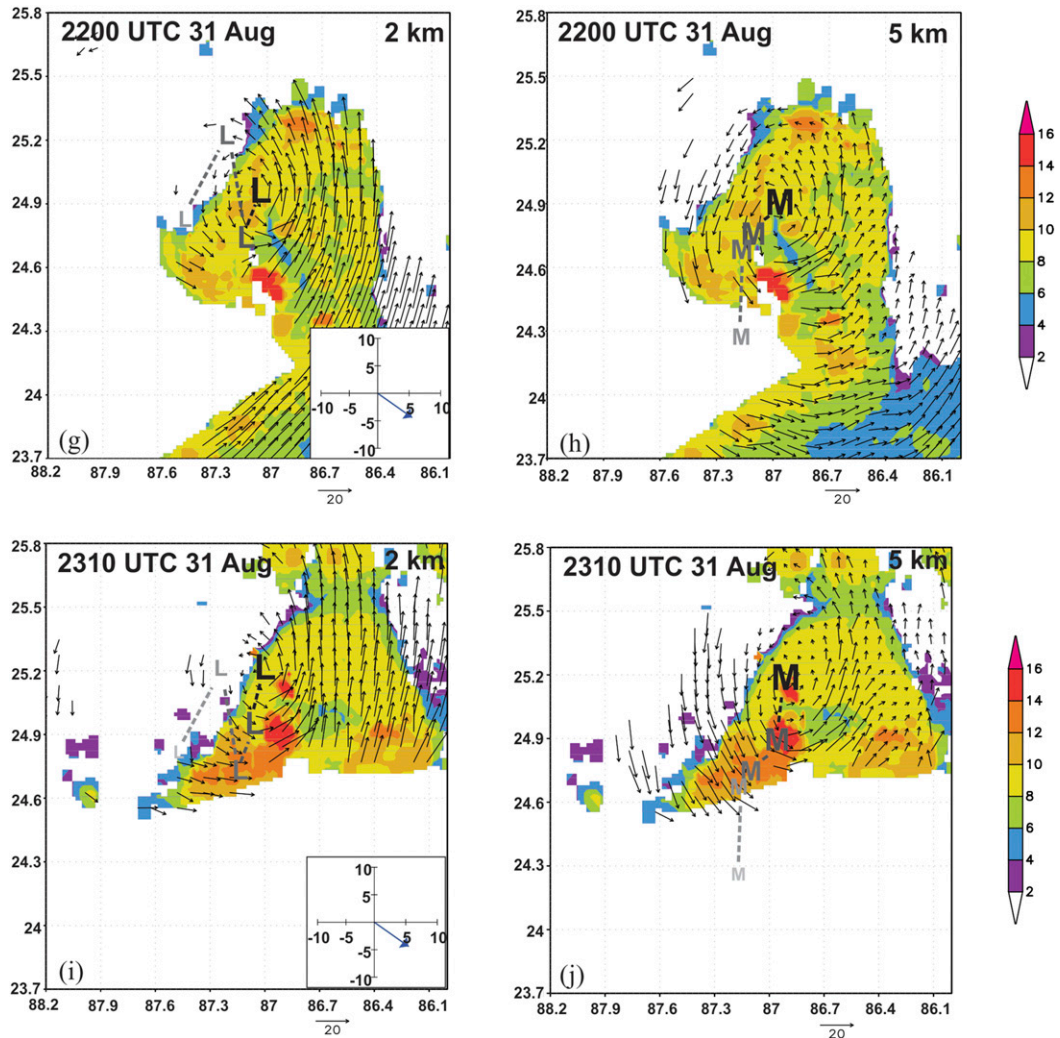


FIG. 6b. (g) As in (a), but for 2200 UTC 31 Aug; (h) as in (b), but for 2200 UTC 31 Aug; (i) as in (a), but for 2310 UTC 31 Aug; and (j) as in (b), but for 2310 UTC 31 Aug. Lighter, smaller letters denote locations from previous radial passes. Inset in lower right corner in (g),(i) denotes SHIPS-derived 850–200-hPa shear, as in Fig. 4.

height of the 20 dBZ echo top, which can serve as a proxy for the depth of convection (e.g., shallow, moderate, deep; Rogers et al. 2016), for each of the five radial passes that comprised 160831I1. Also noted on Fig. 6 are approximate locations of circulation centers at 2 and 5 km, as well as locations of the centers from the previous radial passes from the same mission, to give a sense of the relative locations of the 2- and 5-km centers and their (presumed) motion. These centers are subjectively determined, providing a reasonable assessment of center location given the coverage and organizational constraints mentioned above (which are magnified when considering only a single radial pass versus a merged analysis). While the uncertainty in these center estimates can be

substantial, they provide an adequate assessment of the relative location of the low- and midlevel centers, and the ability to monitor their evolution over near-convective time scales outweighs the drawbacks associated with this uncertainty.

During the first center pass of 160831I1, centered at 1742 UTC, there were widespread areas of shallow and moderate precipitation, with echo tops reaching 4–6 km, and some localized areas of deep convection, with echo tops 10–12 km. One area of deep convection was located ~40 km to the south of the low-level circulation center (identified with a “L” in Fig. 6a), while another area of deep convection was seen ~100 km to the northeast of the low-level center. The midlevel circulation center during this

first pass (identified as “M” in Fig. 6b), was located ~60 km to the south-southeast of the low-level center. Note that the displacement magnitude during this radial pass was less than what was seen from the merged analysis of the previous mission 160830I2 (cf. Fig. 4c), indicating that the two centers were closer to alignment at the start of 160831I1 than ~20 h previously. The second pass (Figs. 6c,d), centered at 1910 UTC, had fewer scatterers and less coverage than the first. The low-level circulation had become elongated in a general north–south orientation. While the locations of a low-level and midlevel center were uncertain with this pass, a reasonable identification of a center to this elongated circulation shows a similar displacement between the approximate location of the low- and midlevel centers as the first pass and they moved toward the north-northeast by ~30 km over the 1.5 h period between the first two passes.

The third pass, centered at 2034 UTC, showed substantial changes (Figs. 6e,f) from the previous two passes. A large area of deep convection with echo tops >14–16 km was evident. An inspection of lower-fuselage radar animations (not shown) suggested that this deep convection developed from the moderate to deep convection south of the low-level circulation seen during the 1742 pass (cf. Figs. 6a,b). The low-level circulation center was coincident with this deep convection, having formed in the southeastern region of the elongated circulation from the previous pass. It was also nearly coincident with the midlevel center. During the next center pass, at 2200 UTC (Figs. 6g,h), the area of deepest convection had diminished, as regions with echo tops of 8–10 km were again prevalent. The fifth and final pass at 2310 UTC showed some localized regions of deeper convection beginning to develop again near the low-level center, and the two centers remained aligned.

Given the evolution of the low- and midlevel centers during the 160831I1 mission shown here, it appears that Hermine achieved a nearly vertically aligned structure through the midtroposphere, suggested by the merged analyses from Fig. 4, during this mission. It also appears that the low-level circulation center shifted to being coincident with the midlevel center. The midlevel centers show a generally steady progression toward the north-northeast, except for a pause in forward motion between the second and third pass, when the deepest convection occurred. By contrast, the low-level centers showed the movement toward the north-northeast between the first and second passes, but then a clear repositioning to the

southeast between the second and third passes. From that point forward the low-level center continued on a movement toward the north-northeast, coincident with the midlevel center. This repositioning of the low-level center appears consistent with previous examples of downshear reformation, where the low-level center reforms underneath a midlevel center in the presence of deep convection and associated stretching of vorticity in the lower troposphere (Molinari et al. 2004, 2006; Molinari and Vollaro 2010; Nguyen and Molinari 2015; Chen et al. 2018). This will be further shown in the next subsections, where the relationship between precipitation structure and vortex alignment will be discussed.

As Fig. 6 showed, there was an apparent relationship between the occurrence of deep convection and the alignment of Hermine. The development of nearly aligned low- and midlevel circulations was first captured by the radar during the third pass of 160831I1, where 20-dBZ echo tops exceeded 16 km at times. Such a relationship between deep convection and vortex development was documented in the observational study of Ophelia (Houze et al. 2009). However, there were other times earlier in Hermine’s life cycle where deep convection occurred that did not result in a sustained period of alignment. One example is shown in Fig. 7, which depicts the 2- and 5-km flow and 20-dBZ echo tops from a center pass at 0957 UTC 30 August during the 160830I1 mission, ~36 h prior to 160831I1. There were two broad regions of deep convection with echo tops exceeding 14–16 km. Despite the presence of deep convection, however, the low-level circulation center was displaced to the northwest (~50 km) of the northern region of deep convection. There did appear to be multiple weak midlevel circulation centers (cf. Figs. 4b, 7b), including a suggestion of a closed circulation (marked by an “M” in Fig. 7b) at the rear edge of the northern region of deep convection. This midlevel circulation, however, was embedded within a broad, elongated cyclonic envelope that was displaced south-southeast (i.e., downshear) of the low-level circulation. Furthermore, by the time of the next mission, ~12 h later (cf. Fig. 4c), there was no indication of a midlevel circulation. The presence of deep convection alone thus did not appear to be sufficient to lead to a persistent, vertically extensive, aligned vortex during this earlier mission. The structure of the precipitation during these two missions, however, may have impacted the structure of the low- and midlevel circulations in Hermine. The potential impact of changes in the precipitation structure on Hermine’s kinematic fields is discussed next.

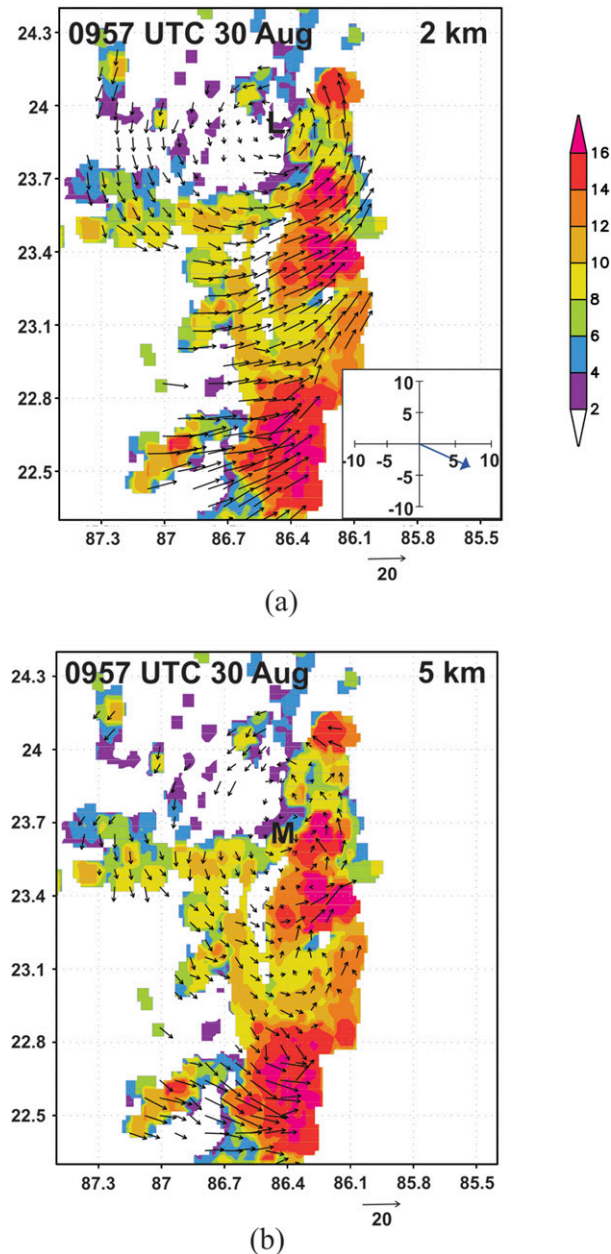


FIG. 7. As in Fig. 6, but for radial pass centered at 0957 UTC 30 Aug. Inset in lower right corner in (a) denotes SHIPS-derived 850–200-hPa shear, as in Fig. 4.

b. Precipitation structure

Figure 8 compares the distribution of precipitation for 160830I1 (when Hermine was a tropical depression with misaligned circulations, hereafter termed mission 2) and 160831I1 (when Hermine became aligned as it was intensifying toward hurricane status, hereafter termed mission 4), using the merged analyses from each of these missions. During mission 2 (Fig. 8a) the majority of

scatterers at 2 km were located southeast (i.e., generally downshear) of the low-level circulation, with widespread areas exceeding 15 dBZ and some localized areas >25 –30 dBZ in this quadrant. During mission 4, 36 h later, most of the precipitation remained concentrated in the southeast (downshear) quadrant. A much broader region of reflectivity >25 –30 dBZ is evident during mission 4 compared to mission 2. Notably as well, much more reflectivity extends to the northwest side (i.e., upshear) of the low-level circulation.

Figures 8c and 8d show vertical cross sections of tangential wind and the coverage of precipitation with reflectivity exceeding 20 dBZ on the downshear side of the low-level center from missions 2 and 4. The tangential wind was negative above ~ 5 km during mission 2, consistent with a misaligned upper-level circulation, while the tangential wind during mission 4 was mostly positive over the depth of the troposphere, consistent with a better-aligned vortex (cf. Fig. 4). During mission 2 there was fairly extensive coverage of precipitation with reflectivity >20 dBZ in the lowest 4 km, with values exceeding 70% coverage extending from ~ 25 –75-km radius downshear. Above the freezing level (typically ~ 5 km altitude; Black and Hallett 1986), there was $>40\%$ coverage of 20+ dBZ reflectivity over a wide radial band. Such coverage extended up to 10 km and above. The precipitation coverage during mission 4 was substantially different, by contrast. In the lower troposphere, precipitation was more widespread, as regions with reflectivity >20 dBZ exceeded 90% coverage between 0- and 75-km radius on the downshear side. At high altitudes, though, there was a much smaller coverage of high reflectivity, with coverage exceeding 20% at one localized region, above 10 km at 25-km radius. Differences in the horizontal and vertical coverage of precipitation between these two missions indicates that mission 2 was comprised of localized areas of deep convection but relatively few areas of shallow and moderate convection (and potentially stratiform precipitation), while mission 4 was comprised of a larger proportion of precipitation of moderate intensity and a smaller (though certainly nonzero; cf. Figs. 6e,f) amount of deep convection.

Statistics of vertical velocity and reflectivity comparing these two missions support this conclusion. Figure 9 shows contoured frequency by altitude diagrams (CFADs; Yuter and Houze 1995) of vertical velocity and reflectivity for a radial pass during missions 2 and 4. No normalization was applied in these CFADs, similar to that done in Rogers et al. (2007, 2012, 2015) and Rogers (2010). Each pass was selected because they had significant coverage of scatterers and contained regions of deep convection as shown in Figs. 6e, 6f and 7.

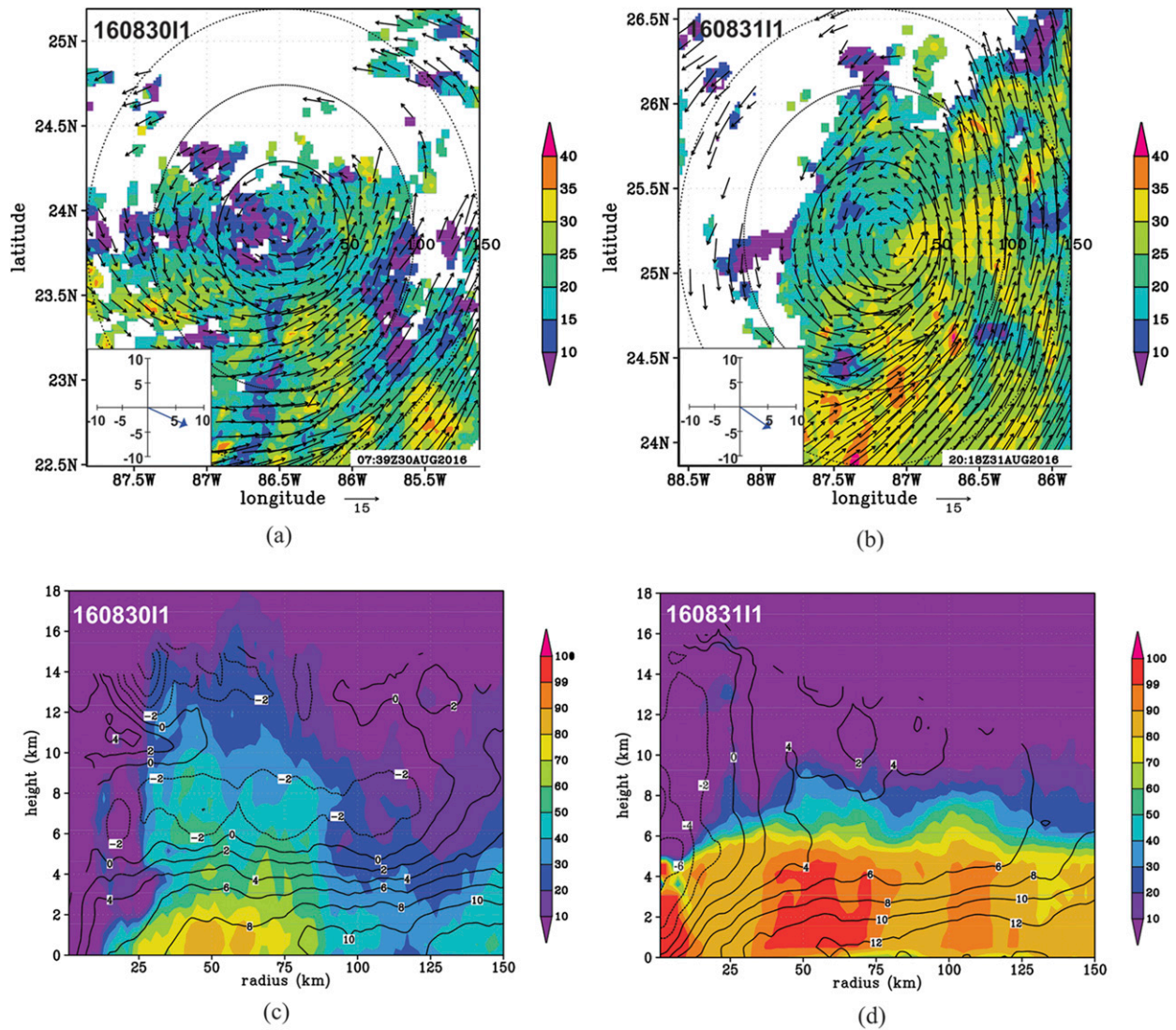


FIG. 8. (a) Reflectivity (shaded, dBZ) at 4-km altitude and storm-relative winds at 2-km altitude (vectors, m s^{-1}) from merged Doppler analysis during mission 160830I1 (mission 2); (b) as in (a), but for mission 160831I1 (mission 4). (c) Coverage of reflectivity >20 dBZ (shaded, percent) and averaged tangential wind (contour, m s^{-1}) on downshear side of Hermine from merged Doppler analysis during mission 160830I1 (mission 2); (d) as in (c), but for mission 160831I1 (mission 4). Inset in lower-left corner in (a) and (b) denotes SHIPS-derived 850–200-hPa shear, as in Fig. 4.

While precipitation evolves over time scales comparable to the separation in time between passes, as will be shown later the relative proportion of precipitation mode remains fairly steady from pass to pass during each mission. The vertical velocity CFAD from mission 2 (Fig. 9a) shows the bulk of vertical velocity between -2 and 2 m s^{-1} , as is typically seen, even for hurricanes (e.g., Rogers et al. 2012). On the extreme ends of the distribution, however, a notable expansion of the vertical velocity distribution was seen with height, with a small percentage of the strongest updrafts (within the 0.2% contour) exceeding 10 m s^{-1} above 10-km altitude. A

broad distribution of downdrafts was also evident, with the bottom 0.1% of the distribution, representing the strongest downdrafts, reaching -4 m s^{-1} over much of the troposphere below 10 km and exceeding -6 m s^{-1} above 12 km. The CFAD for mission 4 (Fig. 9c) shows a narrower vertical velocity distribution, with the highest percentages $>30\%$ within $\pm 0.5 \text{ m s}^{-1}$. The 0.5% contour, indicative of strong updrafts, ranges between 3 and 4 m s^{-1} above 4-km altitude. This is in marked contrast to mission 2, which shows the 0.5% contour increasing from 4 m s^{-1} at 4-km altitude to 8 m s^{-1} at 12 km, indicating that the pass during mission 2 had stronger peak

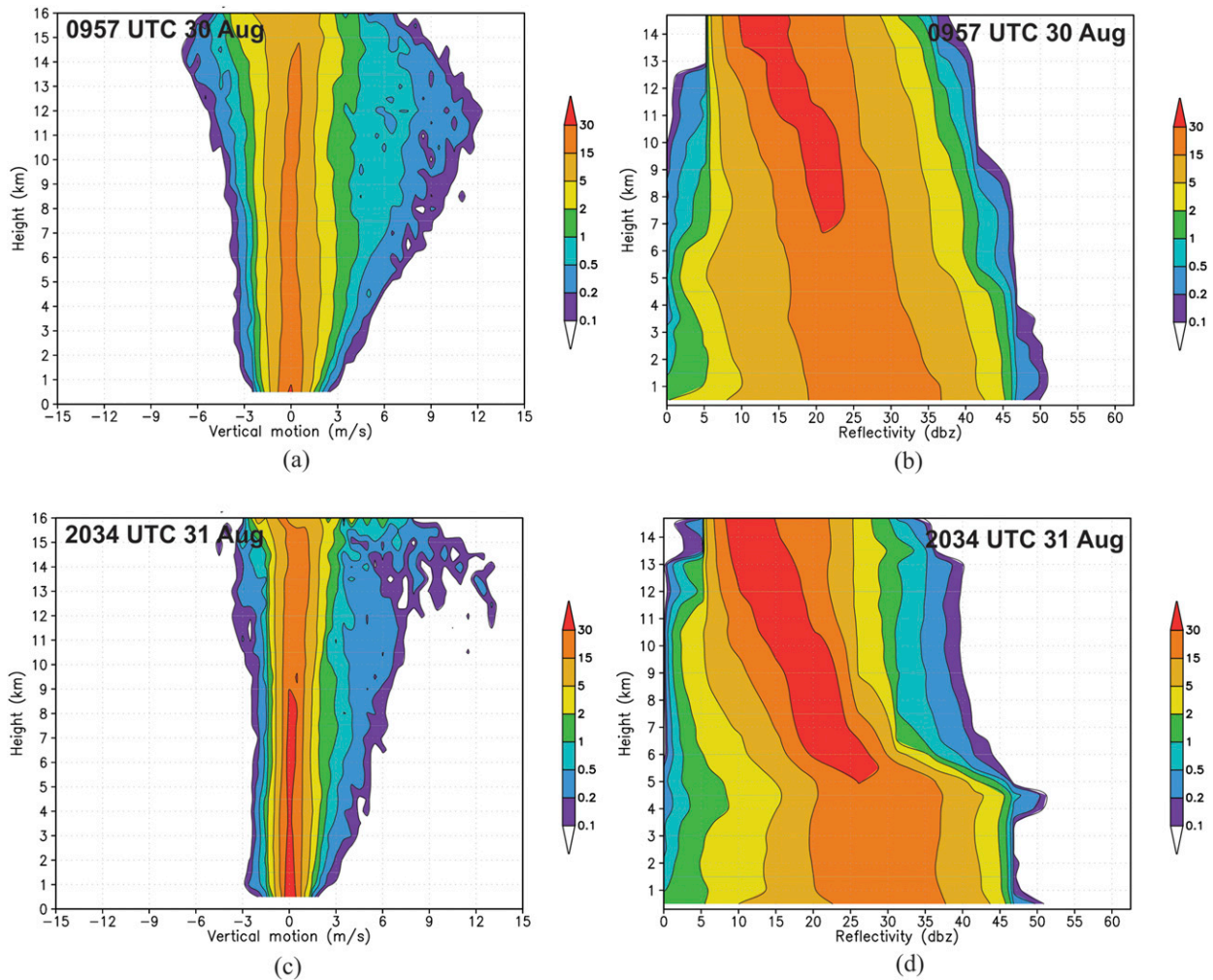


FIG. 9. (a) Contoured frequency by altitude diagram (CFAD) of vertical velocity (shaded, percent) from Doppler analysis domain during radial pass centered at 0957 UTC 30 Aug from mission 16083011 (mission 2); (b) As in (a), but for reflectivity; (c) as in (a), but for radial pass centered at 2034 UTC 31 Aug from mission 16083111 (mission 4); and (d) as in (b), but for radial pass centered at 2034 UTC 31 Aug.

updrafts and deeper convection. The strongest downdrafts did not exceed -3 m s^{-1} over most of the troposphere during mission 4, and only reached -4 m s^{-1} above 12 km, indicating mission 4 had weaker downdrafts than mission 2.

The reflectivity CFAD from the mission 2 pass (Fig. 9b) shows modal values of 25–30 dBZ in the lowest 2 km decreasing steadily with height to a value of ~ 15 dBZ at 14 km. Peak values of reflectivity exceeded 50 dBZ in the lowest 4 km and remain high (above 40 dBZ) over the depth of the troposphere. There is little indication of a sharp reduction of reflectivity above the freezing level, suggesting that vigorous updrafts extended across a deep layer, including across the freezing level, a structure characteristic of deep convection. For the mission 4 pass

(Fig. 9d), lower-tropospheric modal values were of a comparable magnitude to that from the mission 2 pass. In contrast to mission 2, the frequency contours below the freezing level were vertical, indicating little change with height of reflectivity in these levels. Above the freezing level, though, the bulk of the distribution showed a sharp decrease in the frequency contours, and they decrease more rapidly with height in the higher altitudes than the mission 2 pass. This structure is more characteristic of precipitation with weaker vertical velocity, which could be either stratiform precipitation or shallow to moderate convection. However, peak reflectivity values (top 0.1%) still remain above 40 dBZ in the higher altitudes, suggesting that some deep convection is embedded in the precipitation.

To gain additional insight into the structure of the precipitation and how it evolved across missions, a convective/stratiform partitioning algorithm was run on the radar retrievals. Originally developed in Steiner et al. (1995) to work with ground-based radar, the algorithm is based on characteristics of the magnitude and horizontal distribution of reflectivity; namely, intensity, peakedness, and surrounding area, to classify locations as either convective, stratiform, weak echo, or no echo. The algorithm has been used with airborne Doppler observations (e.g., Didlake and Houze 2009) as well as numerical model output (e.g., Rogers 2010). Specific threshold values and formulations used here were modified from that used in Steiner et al. (1995) to account for differences in the airborne radar characteristics and its associated analysis (e.g., sensitivity, attenuation, calibration error, and automated noise removal) compared to the ground-based radar used in the development of the Steiner et al. algorithm. These modifications include 1) a change in the threshold value of reflectivity to identify a location as convective (35 dBZ here; 40 dBZ in Steiner et al.); 2) a change in the threshold reflectivity below which unclassified locations are identified as weak echo (15 dBZ here; 20 dBZ in Steiner et al.); 3) the relationship between the peakedness value (ΔZ) required to identify a location as convective as a function of the background reflectivity [Z_{bg} ; compare with Eq. (2) in Steiner et al.]:

$$\begin{aligned} 15, & \quad Z_{bg} < 0 \\ \Delta Z = 15 - \frac{Z_{bg}^2}{81.67}, & \quad 0 \leq Z_{bg} < 35 \\ 0, & \quad Z_{bg} \geq 35. \end{aligned} \quad (1)$$

These values were arrived at iteratively such that the objective classification of reflectivity was consistent with subjective classifications using vertical cross sections of reflectivity, in a manner similar to that done in Didlake and Houze (2009).

Once the precipitation is partitioned into convective and stratiform precipitation (in addition to weak and no echo), the convective regions are further partitioned into shallow, moderate, and deep convection. This partitioning is based on the height of the 20 dBZ echo top, with echo tops ≤ 6 km deemed shallow convection, tops between 6 and 10 km inclusive deemed moderate convection, and tops above 10 km deemed deep convection, in a methodology similar to Tao and Jiang (2015) and Fritz et al. (2016). Figure 10 shows the results of the partitioning algorithm for the radial passes from missions 2 and 4 discussed above. Both passes show a

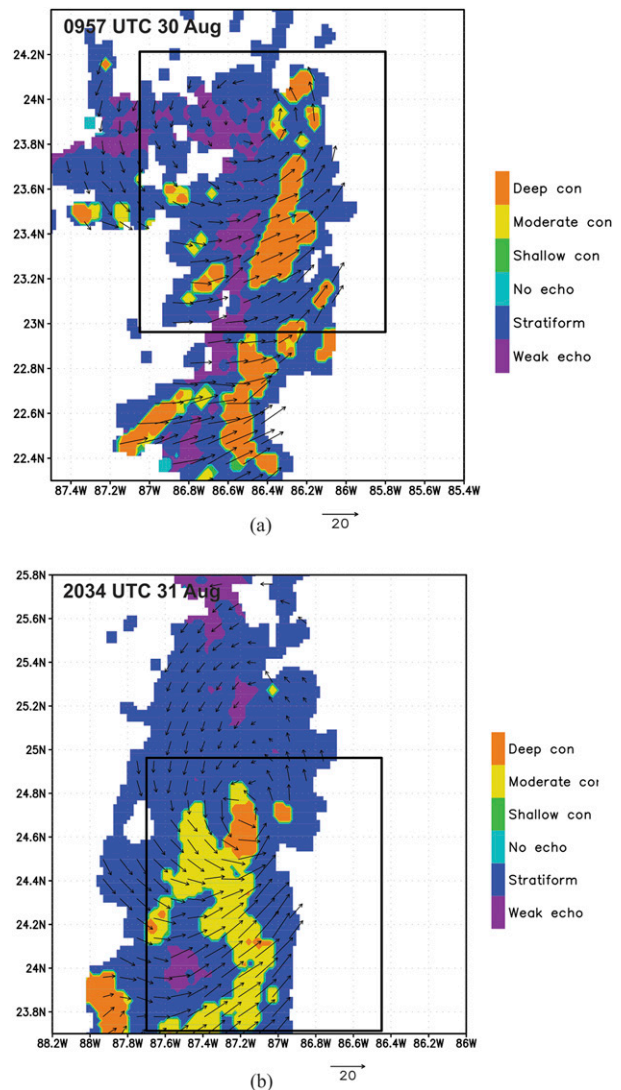


FIG. 10. (a) Results from precipitation classification algorithm (shaded, categories labeled in color bar) and storm-relative flow at 2-km altitude for radial pass centered at 0957 UTC 30 Aug from mission 160830I1 (mission 2); (b) as in (a), but for radial pass centered at 2034 UTC 31 Aug from mission 160831I1 (mission 4).

preponderance of stratiform precipitation, and a small area of weak echo (though mission 2 shows more weak echo than mission 4). What distinguishes the two passes are the relative proportions of deep versus moderate convection. The pass from mission 2 shows broad regions of deep convection and isolated areas of moderate convection. Much of the deep convection is oriented in a generally north-northeast–south-southwest oriented line south (downshear) of the low-level circulation center. The pass from mission 4 shows a much larger proportion of moderate convection, though there are still some regions of deep convection,

TABLE 3. Percent coverage of precipitation modes (stratiform; weak echo; shallow, moderate, deep convection) from P-3 airborne Doppler radar for individual radial passes, and average for each mission, from missions 2, 3, and 4. Note numbers do not always add up to 100% for any given pass due to rounding and the lack of inclusion of the “no echo” category. Italicized values represent the average of the individual passes for that mission.

Mission number	Mission ID	Time of center pass (UTC)	Precipitation mode				
			Stratiform	Weak echo	Shallow convection	Moderate convection	Deep convection
2	160830I1	0720	57.1	33.9	0.3	1.8	6.5
2	160830I1	0847	67.0	22.2	0.6	1.9	8.4
2	160830I1	0957	65.8	16.9	0.1	4.0	13.2
		Average	63.3	24.3	0.3	2.6	9.4
3	160830I2	1756	53.5	38.8	0.6	1.2	0.1
3	160830I2	2303	53.5	36.3	0	2.6	6.0
		Average	53.5	37.6	0.3	1.9	3.1
4	160831I1	1742	69.2	9.0	2.1	18.0	1.7
4	160831I1	2034	64.9	3.7	0.7	26.6	4.1
4	160831I1	2200	62.9	6.3	0.3	28.1	2.3
		Average	65.7	6.3	1.0	24.2	2.7

including the area essentially collocated with the low-level circulation center.

Table 3 shows the percentages of the various precipitation modes from individual radial passes for missions 2, 3, and 4. These percentages are calculated for a $1.25^\circ \times 1.25^\circ$ box shifted ~ 25 km south-southeast of the low-level center for each pass, to incorporate a greater proportion of the downshear environment based on the 850–200-hPa shear vectors (cf. Fig. 4) while still including the low-level and as much of the midlevel center (to the extent that a midlevel center can be defined for the earlier missions) as possible. For all three missions stratiform precipitation comprises the majority of precipitation, at $\sim 55\%$ – 65% of the precipitating area. Such a large percentage of stratiform rainfall reflects the importance of stratiform precipitation in TC intensification, as shown in composites of rapidly intensifying TCs using the TRMM Precipitation Radar (Zagrodnik and Jiang 2014; Tao et al. 2017). Mission 2 has a sizable proportion of convection, and most of that is deep convection, with an average of $\sim 9\%$ of the total precipitation coverage classified as deep convection and $\sim 3\%$ classified as moderate convection. While these numbers are averages across three passes, the ratio of deep to moderate convection remains relatively unchanged from pass to pass. Mission 3, occurring during the late afternoon hours of ~ 1800 – 2300 UTC 30 August, is during what is typically a diurnal minimum in convective activity (Leppert and Cecil 2016), and hence has the highest percentage of weak echo and limited coverage of convection of all types. Mission 4 has a sizable proportion of convection — more than mission 2 — even though mission 4 also occurred during the expected diurnal minimum. Mission 4 also has a significantly reduced percentage of weak echo compared to mission 2.

Strikingly, the vast majority of convection during Mission 4 is classified as moderate convection, with $\sim 24\%$ classified as moderate convection and $\sim 3\%$ classified as deep convection. Note that, similar to mission 2, this relationship holds from pass to pass during mission 4, indicating that these percentages of deep versus moderate convection from both missions likely do not represent different stages of convection in the evolution of a mesoscale convective system. Rather, they likely represent a response of the convection during each of these missions to the local thermodynamic environment downshear.

Figure 11 presents this local thermodynamic environment as indicated by profiles from dropsondes released by the Global Hawk (GH) within a 200-km radius circle (indicated in Figs. 2c,d) centered on the approximate location of the midlevel circulation (which is biased to the downshear side during both GH missions). The profiles colored black are during the early GH mission, which is roughly during the time of mission 2, while the blue profiles are when the GH was sampling Hermine during mission 4. The profile of relative humidity from the early GH mission shows values near 90% in the lowest 2 km, but they drop below 80% at 4 km and down to 50% by 8 km altitude. The profile from the late mission has the same humidity below 2 km, but the profile is markedly moister above that altitude, remaining above 80% up to 8 km. The temperature anomaly from the early GH mission shows a weak warm anomaly below the freezing level and a negligible anomaly above that, while the late GH mission shows a shallow surface-based cold anomaly and a pronounced warm anomaly above 6 km. The conditional stability of the troposphere can be determined by comparing the θ_e of a pseudoadiabatically lifted parcel (i.e., θ_e held

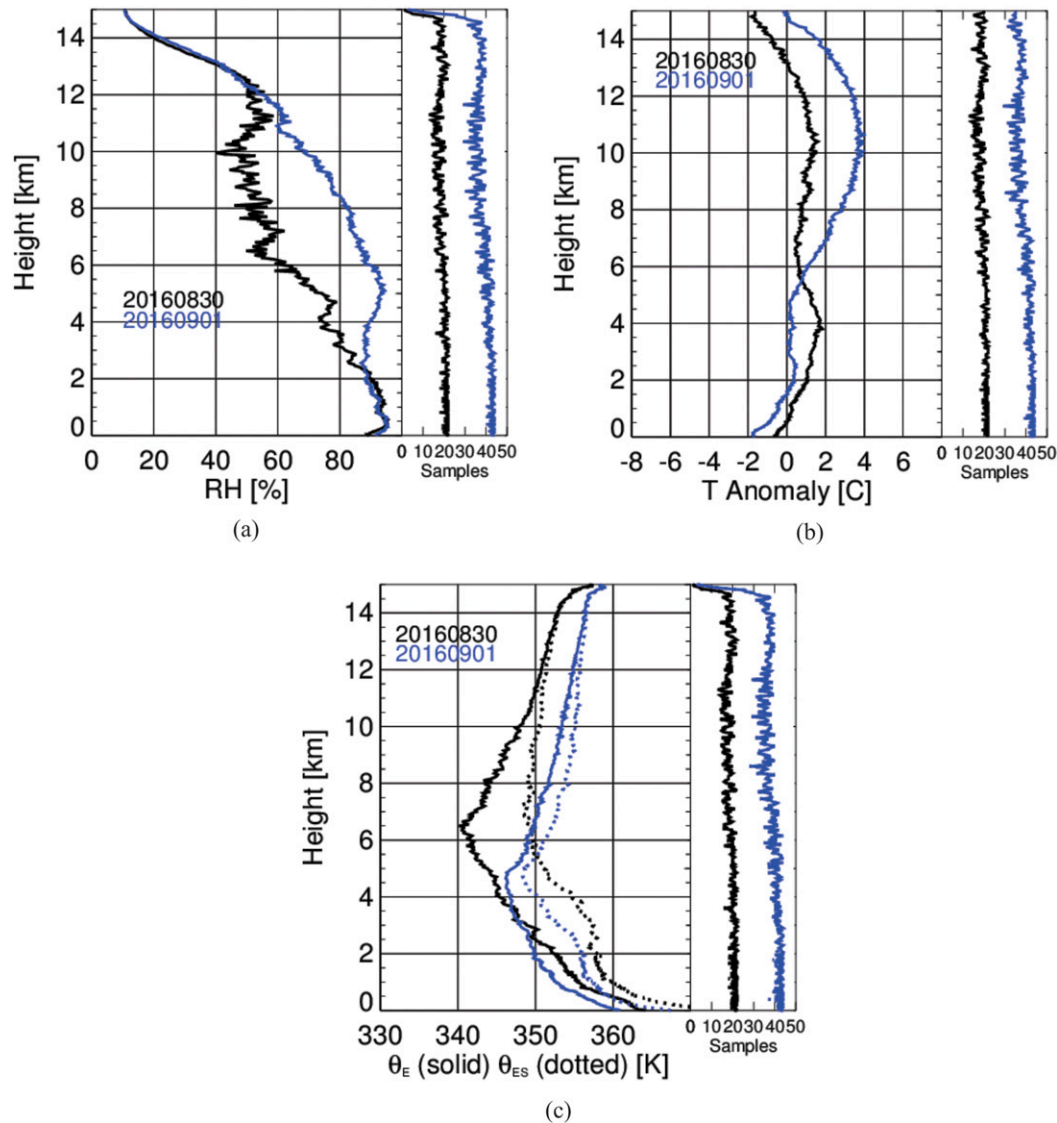


FIG. 11. (a) Profile of average relative humidity from Global Hawk (GH) dropsondes averaged in a 200-km radius circle centered at the midlevel center. Black (blue) profiles denote averages from the 30 Aug (1 Sep) missions. (b) As in (a), but for temperature anomaly (environmental temperature defined as average of GH sondes within 300–700 km annulus). (c) As in (a), but for equivalent potential temperature (solid lines) and saturated equivalent potential temperature (dotted lines).

constant as the parcel rises) with the θ_{es} of its immediate environment at a given altitude (Holton 2004; Nguyen et al. 2017, 2019). Comparisons of the equivalent and saturated equivalent potential temperature (Fig. 11c) show that the environment from the early GH mission is much more unstable than that from the late mission, even factoring in the dilution of updrafts likely to occur in the dry environment depicted in Fig. 11a. While still showing instability during the late mission, the environment is notably more stable compared with that from the early mission. In summary, the

downshear thermodynamic environment of the early GH mission during mission 2 is dry, has a weak (or nonexistent) temperature anomaly, and is unstable. By contrast, the downshear environment of the late GH mission during mission 4 is moist over a deep layer, has a well-developed warm anomaly aloft, and is less unstable.

The differences in the thermodynamic environment downshear as revealed by the GH dropsondes are consistent with the differences in the radar-derived structure of the precipitation for missions 2 and 4. The more

unstable environment during mission 2 is supportive of strong updrafts and deep convection, but the detrainment from convective towers in the mid to upper-level dry air leads to strong downdrafts at those altitudes. By contrast, during mission 4 the environment is unstable in the lowest 5 km, but above that the temperature anomaly has warmed and the equivalent potential temperature profile has become significantly more stable. Convection in this environment will thus be shallower. The moister environment, however, will result in weaker downdrafts and fewer weak echoes throughout the troposphere. All of these relationships are borne out by the CFADs shown in Fig. 9, as well as the relative proportion of deep versus moderate convection and weak echoes seen in Fig. 10 and Table 3.

c. Multiscale contributions to development of aligned vortex

A key step in the intensification of Hermine is the development of an aligned vortex, as shown in the evolution of the merged analyses in Fig. 4. However, a temporal gap of ~ 20 h (cf. Table 1, Fig. 1) of Doppler radar sampling precludes a definitive assessment of when the low- and midlevel vortices came closer into vertical alignment. A more finescale temporal analysis during mission 4 (cf. Fig. 6) shows that deep convection appears to be associated with the repositioning of the low-level circulation center underneath an existing midlevel center. A similar shifting of the low-level center toward the location of deep convection, similar to that seen in simulations of Typhoon Vicente (Chen et al. 2018), was evident in previous missions (not shown), but there was never an alignment, and the repositioning evidently did not persist. A comparison of the structure of the convection within and downshear of the low-level circulation showed a distinct transition from one dominated by deep convection during missions 2 and 3 to one characterized primarily by moderate convection during mission 4 (both periods had comparable amounts of stratiform precipitation). In this subsection the impact of these different modes of convection on the development of an aligned vortex is examined, both within the context of convective-scale adjustments as well as its mesoscale impacts on the broader circulation.

1) CONVECTIVE-SCALE CONTRIBUTIONS

Figure 12 shows plan view plots of reflectivity, vorticity, and winds at 2 and 5 km, along with vertical cross sections of reflectivity, vertical velocity, vorticity, divergence, and precipitation mode during the mission 2 pass shown in Figs. 7 and 10. A north–south line of high reflectivity classified primarily as deep convection (cf. Fig. 10) extends ~ 150 km south of the low-level center.

At 5 km the flow field is diffuse, but there is a broad (spanning $\sim 1.3^\circ$ latitude, or ~ 150 km diameter) cyclonic circulation located downshear of the low-level center. Embedded within this circulation are localized areas of high vorticity associated with regions of deep convection. An east–west cross section (Figs. 12c,d) is taken through the northern area of deep convection, through the approximate center of the broad midlevel circulation and within ~ 70 km of the low-level circulation. The region of deep convection has extensive regions of reflectivity >40 dBZ in the lower troposphere and peak updrafts >8 m s $^{-1}$ above 10 km. Trailing that convection to the west is subsidence reaching -4 m s $^{-1}$, which could be due to detrainment from the updrafts and subsequent evaporation and sublimation in dry environmental air horizontally intruding into the local environment from the upshear regions. A weak echo region is located within the area of subsidence, with a small region of moderate convection and stratiform precipitation farther west. Vorticity is maximized in the midlevels and located within the deep convection. Weak convergence is occurring throughout the lower troposphere in the deep convection and is maximized just below the peak midlevel vorticity, with strong divergence aloft. Winds in the plane of the cross section (Fig. 12c) show strong westerly flow below 4 km and weaker, and even easterly, flow above that (a pronounced southerly component to the winds below 4 km (not shown) is also apparent). This flow change with height, which may reflect the displacement of the circulations as well as divergence from the deep convection, indicates vertical shear in the local environment of the deep convection.

To assess the primary contributors to vorticity sources/sinks and advection in the local environment of the midlevel vortex and deep convection, Fig. 13 shows terms from the advective form of the vorticity budget equation that considers contributions to the Eulerian tendency in relative vertical vorticity from horizontal and vertical advection, stretching, and tilting (Nguyen and Molinari 2015; Fang and Zhang 2010):

$$\frac{\partial \zeta}{\partial t} = -(V_h - C) \cdot \nabla_h (\zeta + f) - w \frac{\partial \zeta}{\partial z} - (\zeta + f) \nabla_h \cdot (V_h - C) - \left(\frac{\partial w}{\partial x} \frac{\partial v}{\partial z} - \frac{\partial w}{\partial y} \frac{\partial u}{\partial z} \right), \quad (2)$$

where ζ is the relative vorticity, V_h is the horizontal storm-relative flow, C is the motion of the TC, f is the Coriolis parameter, ∇_h is the horizontal gradient operator, and (u, v, w) are the three-dimensional storm-relative flow components. The terms on the right-hand side of the equation represent horizontal advection of absolute vorticity, vertical advection of absolute vorticity,

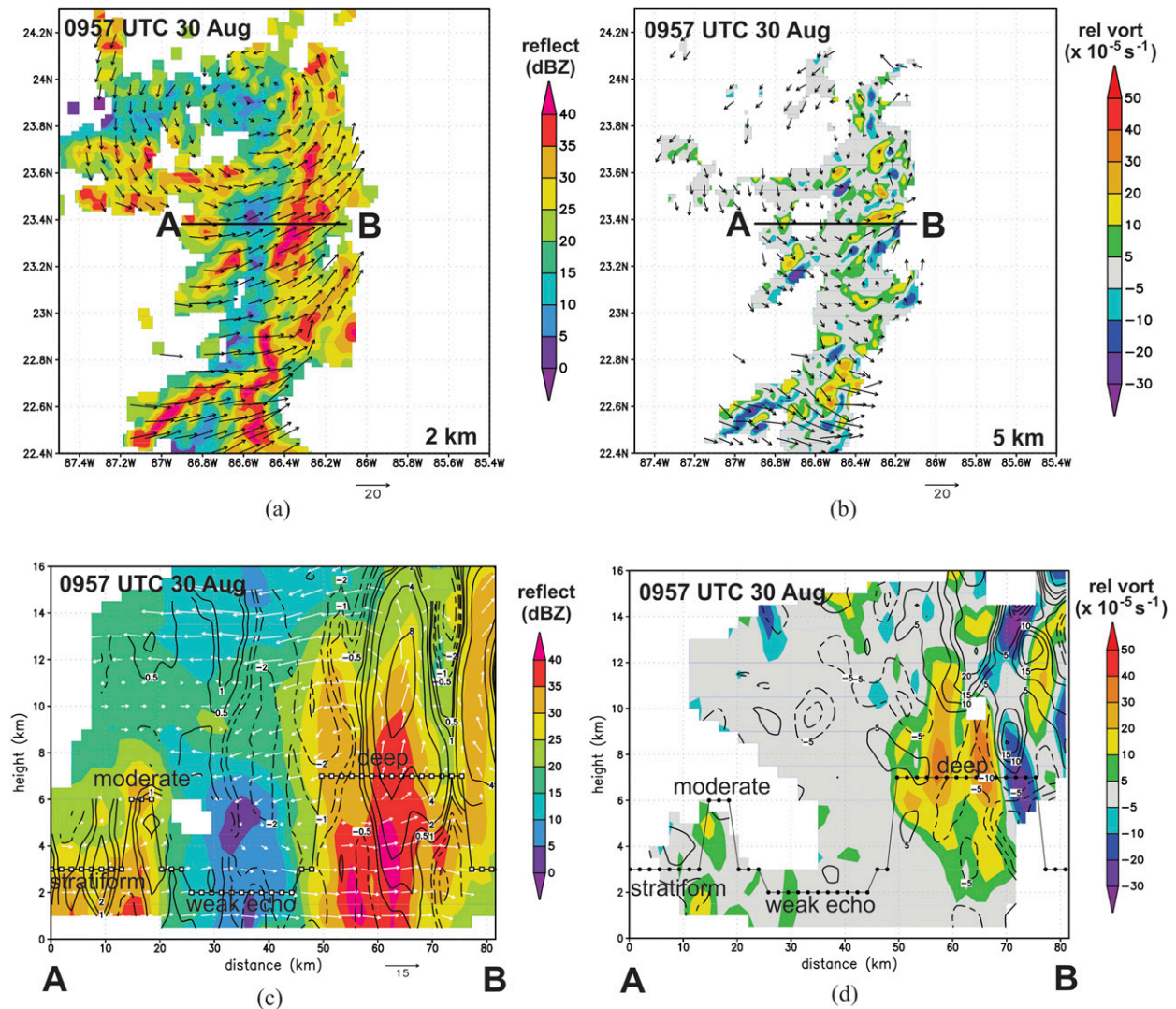


FIG. 12. (a) Reflectivity (shaded, dBZ) and storm-relative winds (vector, m s^{-1}) at 2-km altitude for radial pass centered at 0957 UTC 30 Aug during mission 16083011 (mission 2). Line AB denotes location of cross section in (c),(d) and Fig. 15. (b) As in (a), but for relative vorticity (shaded, $\times 10^{-5} \text{ s}^{-1}$) and storm-relative winds at 5-km altitude. (c) Vertical cross of reflectivity (shaded, dBZ), vertical velocity (contour, m s^{-1} ; note nonuniform contour levels), and storm-relative winds (vector, m s^{-1}) in plane of cross section. Locations of precipitation mode classification indicated on cross section. (d) As in (c), but for relative vorticity (shaded, $\times 10^{-5} \text{ s}^{-1}$) and divergence (contour, $\times 10^{-5} \text{ s}^{-1}$).

stretching of absolute vorticity, and tilting of horizontal vorticity into the vertical. As in many other studies (e.g., Cram et al. 2002; Nguyen and Molinari 2015) the solenoidal term (not shown) is neglected. While it is impossible to calculate a closed budget with Doppler radar data with limited, variable spatial and temporal coverage, it is nevertheless useful to examine the magnitude of the source/sink (stretching and tilting) and advection (horizontal and vertical) terms at the time of the pass. During the mission 2 pass negative contributions from horizontal advection are seen in the mid to upper troposphere in the region of deep convection. In the

advective form, this negative tendency is partially offset by the positive vertical-advective tendency. Stretching has a positive contribution as well in the deep convection, but it is maximized in the midtroposphere coincident with the regions of highest vorticity and convergence (cf. Figs. 12d, 13d). There is also an area of weak positive contribution from stretching in the lower troposphere in the deep convection, but its magnitude is limited from the lack of vorticity in the low levels coupled with weak convergence there. Tilting shows a positive contribution in the deep convection between 4 and 7 km, which is likely due to strong vertical velocity

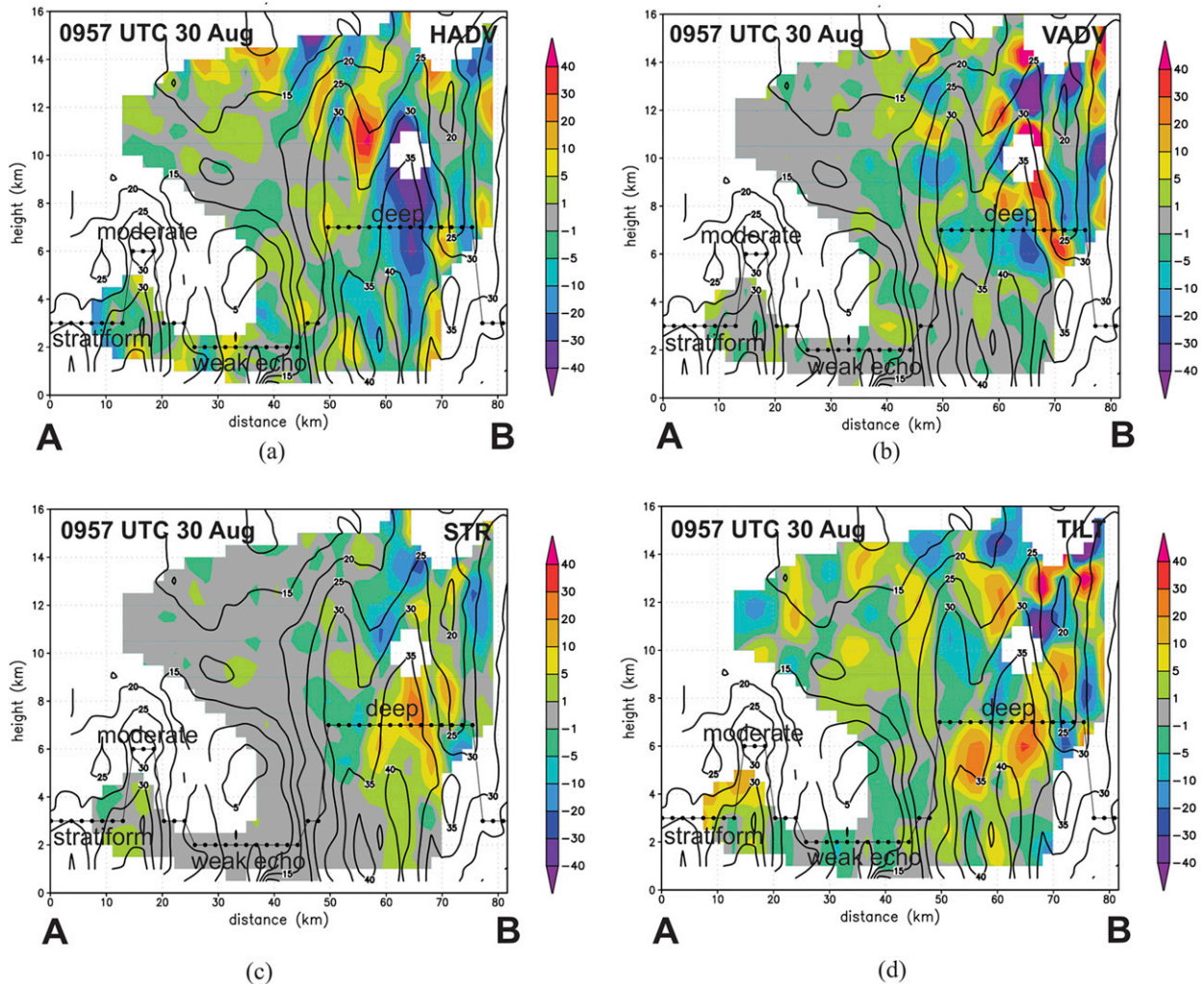


FIG. 13. Vertical cross section of contribution to absolute vorticity tendency (shaded, $10^{-5} \text{ s}^{-1} \text{ min}^{-1}$) from (a) horizontal advection, (b) vertical advection, (c) stretching, and (d) tilting from radial pass centered at 0957 UTC 30 Aug from mission 160830I1 (mission 2). Contours denote reflectivity; locations of precipitation mode classification indicated on cross section.

in the presence of vertical shear of the horizontal flow both along (cf. Fig. 12c) and perpendicular to (not shown) the plane of the cross section.

A similar analysis is performed for the pass from mission 4 (Figs. 14, 15). High reflectivity at 2 km is again preferentially located downshear of the low-level circulation, but there is a greater coverage of precipitation throughout the domain, similar to what was shown in Fig. 8. A vertical cross section, again passing through the midlevel circulation center, shows that the western area of highest reflectivity is classified as moderate convection (cf. Fig. 10b), though the area associated with the (now nearly aligned) low- and midlevel circulations is classified as deep convection. Midlevel vorticity is more consolidated now and is located near the midlevel circulation center. High reflectivity in the low levels is

again seen in the deep convection, with strong updrafts exceeding 12 m s^{-1} occurring at 12 km and a limited region of subsidence around the periphery of the updraft core. Stratiform precipitation and moderate convection fill out the rest of the cross section, with no weak echo region detected. The vorticity now extends over a much deeper layer and is maximized in the lowest 3 km. Convergence is also maximized in the low levels and extends up to a high altitude, with strong divergence above 12 km. The flow field continues to show the strongest westerly flow in the lowest 4 km and weaker flow aloft.

Terms from the vorticity budget (Fig. 15) show generally opposing tendencies from horizontal and vertical advection in the deep convection below 6 km. Stretching is substantial in the lowest 4 km, and

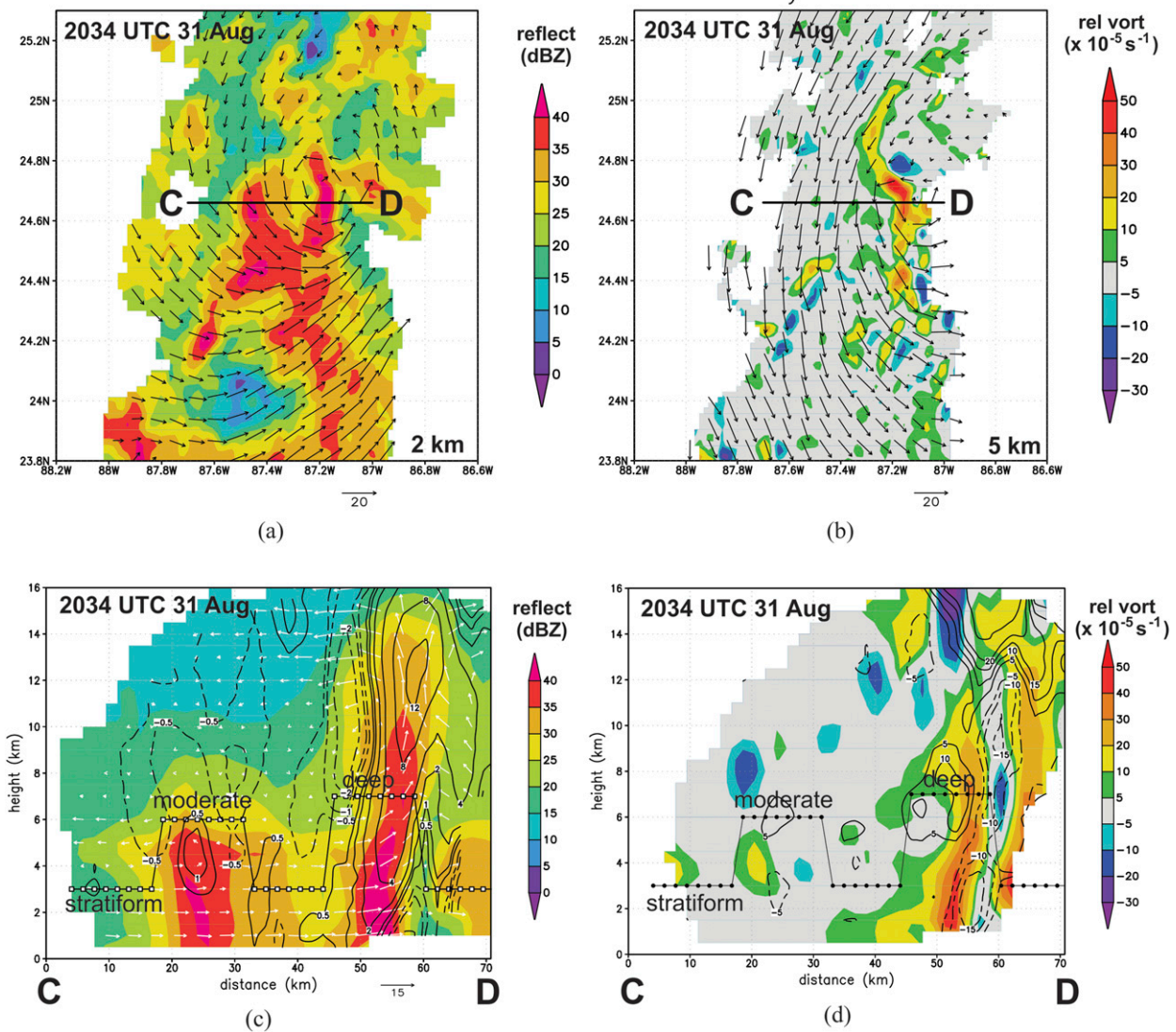


FIG. 14. As in Fig. 12, but for radial pass centered at 2034 UTC 31 Aug from mission 160831I1 (mission 4).

much higher than during the Mission 2 pass, in the deep convection. The maximum in stretching is collocated with the overlap in strong convergence and high low-level vorticity seen at $r \sim 52 \text{ km}$ in Fig. 14d. Additionally, there is a well-defined couplet from the tilting term between 2 and 6 km, with the positive contribution adjacent to the positive contribution from the stretching term, again likely associated with strong vertical velocity in the presence of along-section (cf. Fig. 14c) and across-section (not shown) vertical shear in the lowest 4 km. Additional contributions are seen in the moderate convection to the west, but they are of a much weaker magnitude than that seen in the deep convection.

A comparison of the structure of convection and their contributions to the vorticity tendency from these

two missions shows that the aligned vortex during mission 4 is associated with significant contributions from stretching and tilting in the lower troposphere in deep convection. There is a much smaller contribution toward increasing low-level vorticity from moderate convection and stratiform precipitation. While deep convection was present during mission 2 (to a greater extent than during mission 4), the stretching and tilting were maximized in the midlevels, collocated with the peaks in midlevel vorticity and convergence. It was not until mission 4 that deep convection led to stretching and tilting in the low levels, resulting in an aligned vortex as seen in Figs. 6e and 6f. It should be noted that the structure of stretching described here was consistent for similar cross sections displaced $\sim 20 \text{ km}$ from those shown in

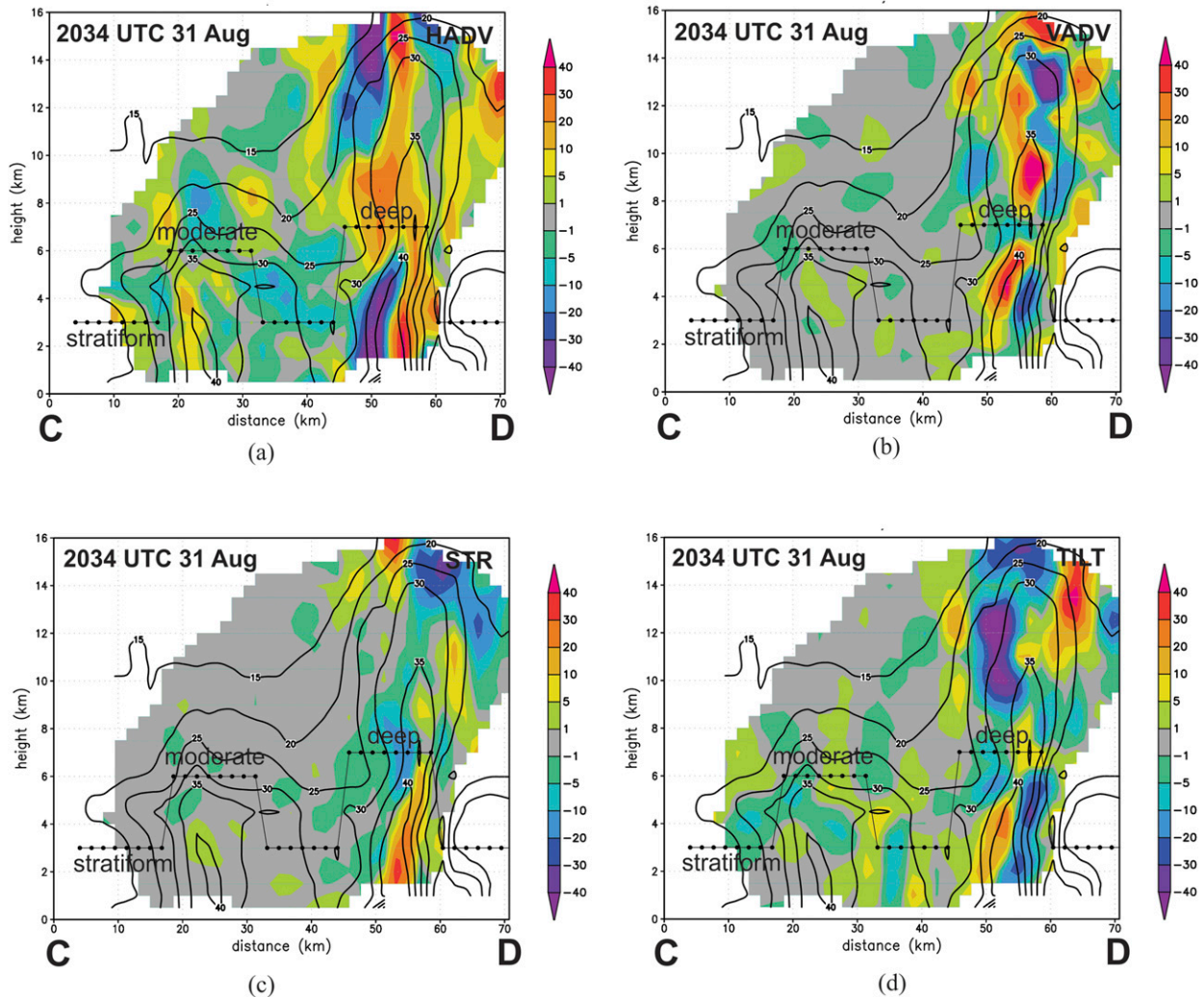


FIG. 15. As in Fig. 13, but for radial pass centered at 2034 UTC 31 Aug from mission 16083111 (mission 4).

Figs. 12 and 14 (not shown), indicating that the differences in these terms between missions 2 and 4 were robust spatially. Similarly, a cross section taken from the radial pass ~ 2.5 h after that shown in Fig. 14 (not shown) shows a local maximum in stretching below 4 km, suggesting that that structure was temporally robust.

2) MESOSCALE IMPACTS

Convective-scale processes modified the structure of the vortex through vortex stretching and tilting as shown in Figs. 12–15. Precipitation processes also impact the system on the mesoscale, providing a pathway for a response of the vortex to the evolving latent heating structure and distribution that persists beyond convective time scales. Figure 16 shows profiles of some key structures related to this pathway. The circulation, shown in Fig. 16a, is calculated as the areal integral of

vorticity (as in Houze et al. 2009) within the $1.25^\circ \times 1.25^\circ$ box shifted downshear to encompass the low-level circulation center and the local environment downshear (cf. Fig. 10). This calculation is performed for the same three passes from missions 2 and 4 that were shown in Table 3. For mission 2 the circulation is maximized within the boundary layer (~ 1 km altitude) and decreases steadily with height, vanishing by ~ 8 km. This is consistent with the shallow vortex shown in Fig. 4. By mission 4 the circulation had increased substantially, both within the boundary layer but also throughout the troposphere. Additionally, a near-constant circulation is evident between 2 and 6 km, before decreasing steadily with height above that. The circulation changes between missions 2 and 4 indicate that the circulation had strengthened in time in the lower and middle troposphere.

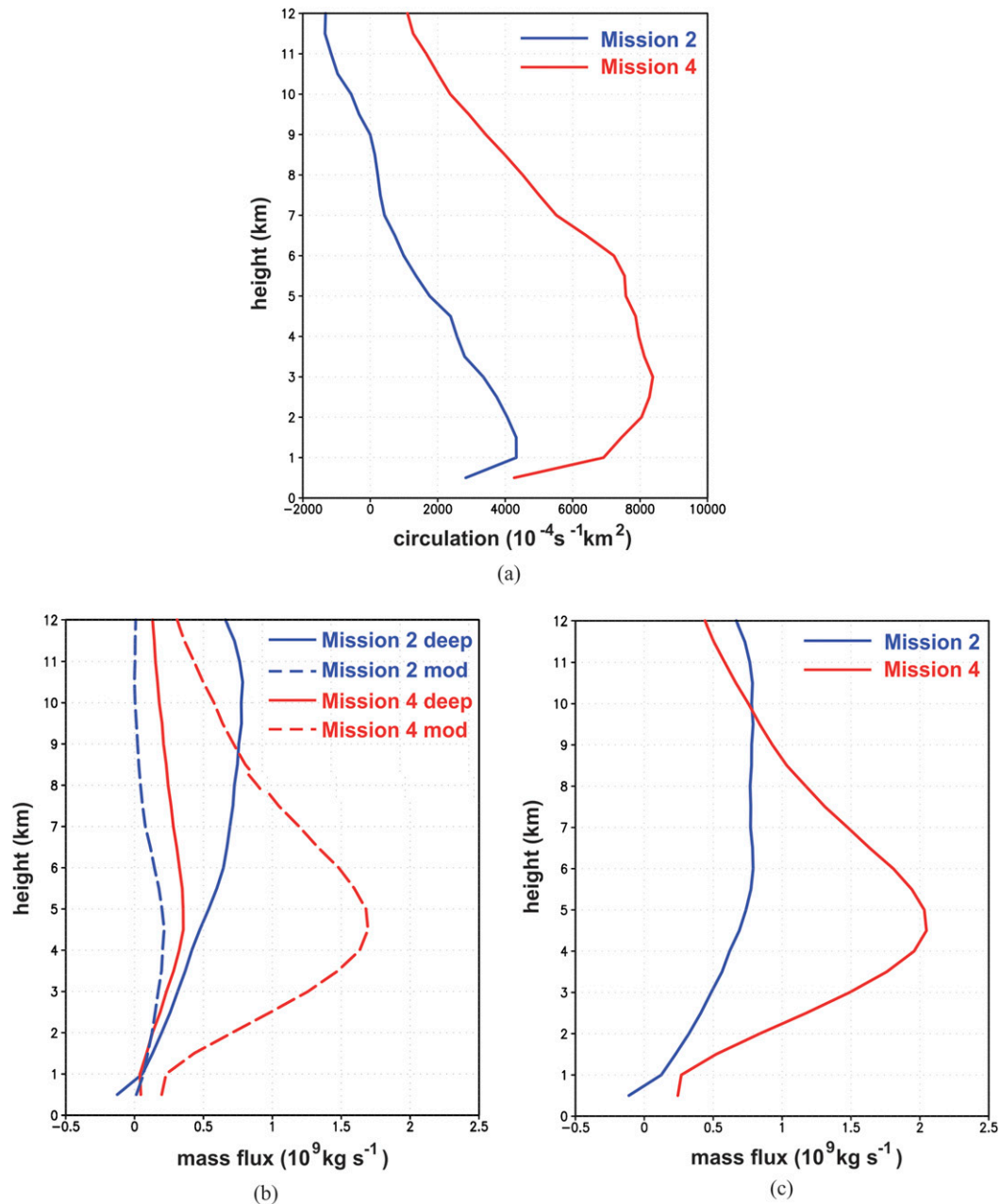


FIG. 16. (a) Total circulation ($\times 10^{-4} \text{ s}^{-1} \text{ km}^{-2}$) per radial pass in $1.25^\circ \times 1.25^\circ$ box incorporating low-level circulation center and downshear environment (see text for details) averaged from three radial passes during mission 2 (160830I1; blue line) and mission 4 (160831I1; red line). (b) Aggregate vertical mass flux ($\times 10^9 \text{ kg s}^{-1}$) per radial pass for regions classified as deep (solid) and moderate convection (dashed) for mission 2 (blue) and mission 4 (red). (c) As in (b), but for sum of mass flux from deep and moderate convection for each mission.

Profiles of vertical mass flux, calculated as the product of vertical velocity, density (calculated as in Hence and Houze 2008), and area are shown in Figs. 16b and 16c for the same passes from missions 2 and 4. Aggregate mass flux is calculated to depict its integrated impacts on the profiles of latent heating and vortex stretching (Houze et al. 2009; Raymond

and López Carrillo 2011; Gjorgjievska and Raymond 2014; Rios-Berrios et al. 2018) within the mesoscale environment at and downshear of the low-level circulation. These variables are further partitioned into the moderate and deep convection categories in Fig. 16b. The deep convective mass flux profile from mission 2 shows a slow, but steady, increase with height, reaching a

peak at 10 km. The moderate convective profile from this same mission shows a peak at $\sim 4\text{--}5$ km – consistent with the shallow depth of reflectivity associated with moderate convection.¹ The combination of the deep and moderate convection yields a total² convective mass flux profile shown in Fig. 16c. The total convective mass flux profile from mission 2 reaches a peak of $0.8 \times 10^9 \text{ kg s}^{-1}$ at ~ 5.5 km and remains close to that value up to 11 km, similar in shape to a “top-heavy” mass flux profile (e.g., Raymond and López Carrillo 2011). Since the vertical gradient in mass flux can be considered a proxy for the production of potential vorticity (e.g., Houze et al. 2009), the relatively weak vertical gradient in mass flux from near the surface up to the peak at 5.5 km indicates weak production of potential vorticity and implies relatively weak vortex stretching over the lower half of the troposphere.

A notably different set of profiles is evident for mission 4. By far the dominant contribution to the aggregate mass flux is from moderate convection. The peak from moderate convection at 4.5 km is more than three times the peak from any other convective mode at that altitude from either mission. The reason for this large contribution in the aggregate mass flux, even though vertical velocities are weaker in moderate convection than deep convection (cf. Figs. 12, 14), is that the moderate convection occupies such a large percentage ($\sim 25\%$; cf. Table 3) of the precipitating area downshear during mission 4. Above 4.5 km the moderate convective profile decreases substantially up to 12 km. Interestingly, the deep convective profile from this mission shows a similar shape (i.e., a peak at ~ 4.5 km and associated decrease above), though its magnitude is much smaller because of the smaller coverage. The total convective mass flux profile for mission 4 shown in Fig. 16c largely mirrors that of the moderate convection. The large vertical gradient in mass flux between 1 and 4.5 km suggests strong vortex stretching in this altitude range, in marked contrast to mission 2.

Figure 17 shows average contributions to local vertical vorticity tendency from the stretching and tilting production terms in deep and moderate convection during the two missions. During mission 2 (Fig. 17a) there is a

small contribution to vorticity tendency from stretching in deep convection within the lowest 2 km, and a similarly small contribution from tilting at ~ 2 km. Above 3 km the tilting contributions in deep convection vary from positive to negative, but contributions from the other terms are negligible until a sharp negative contribution from stretching compensated by positive tilting from deep convection above 10 km. During mission 4 (Fig. 17b) a pronounced positive contribution from stretching is evident from 1 to 4 km in both deep and moderate convection. There is also a positive contribution from tilting in the deep convection, but this is largely offset by a negative contribution in moderate convection above 2 km. Above 4 km the stretching contribution is negative from both deep and moderate convection. The combined contributions from both production terms in both modes of convection for the two missions are shown in Fig. 17c. Both missions show positive production of vorticity in the lower troposphere, but the production during mission 4 is nearly three times that during mission 2. The dominant contributions during mission 4 are from stretching in both deep and (particularly) moderate convection, as well as tilting in deep convection. There is a pronounced negative contribution peaking at 6 km, largely from stretching in moderate convection. This negative production, however, is countered by horizontal and vertical advection (profiles not shown; cf. Fig. 15a for examples along a cross section).

4. Discussion and conclusions

The long period of time Hermine took to intensify is reflective of the marginal environment in which it was embedded. Despite the uncertainty inherent in such an environment, there were some distinct characteristics of Hermine’s inner-core and near environmental kinematic, thermodynamic, and precipitation structure and evolution that facilitated the alignment and deepening of Hermine, setting the stage for intensification. These characteristics are discussed within the framework of the three questions presented in the introduction.

a. Discussion of questions from introduction

1) WHAT WAS THE EVOLUTION OF THE LOW- AND MIDDLELEVEL CIRCULATIONS DURING HERMINE’S DEVELOPMENT?

The analysis of Hermine shown here technically did not show genesis, as it involved an existing long-lived low-level circulation center rather than the development of such a low-level circulation. In the case of Hermine, the midlevel circulation center was transient, or it was at

¹ Profiles for the stratiform region are not shown, for two reasons: 1) the percentages of stratiform coverage are nearly identical (63.3% and 65.7%; cf. Table 3) for missions 2 and 4; and 2) uncertainties in the retrieval of vertical velocity (Rogers et al. 2012) are of comparable magnitude to the weak vertical velocities typically accompanying stratiform precipitation.

² Since such a small percentage ($\leq 1\%$) of the area was occupied by shallow convection, this was not shown.

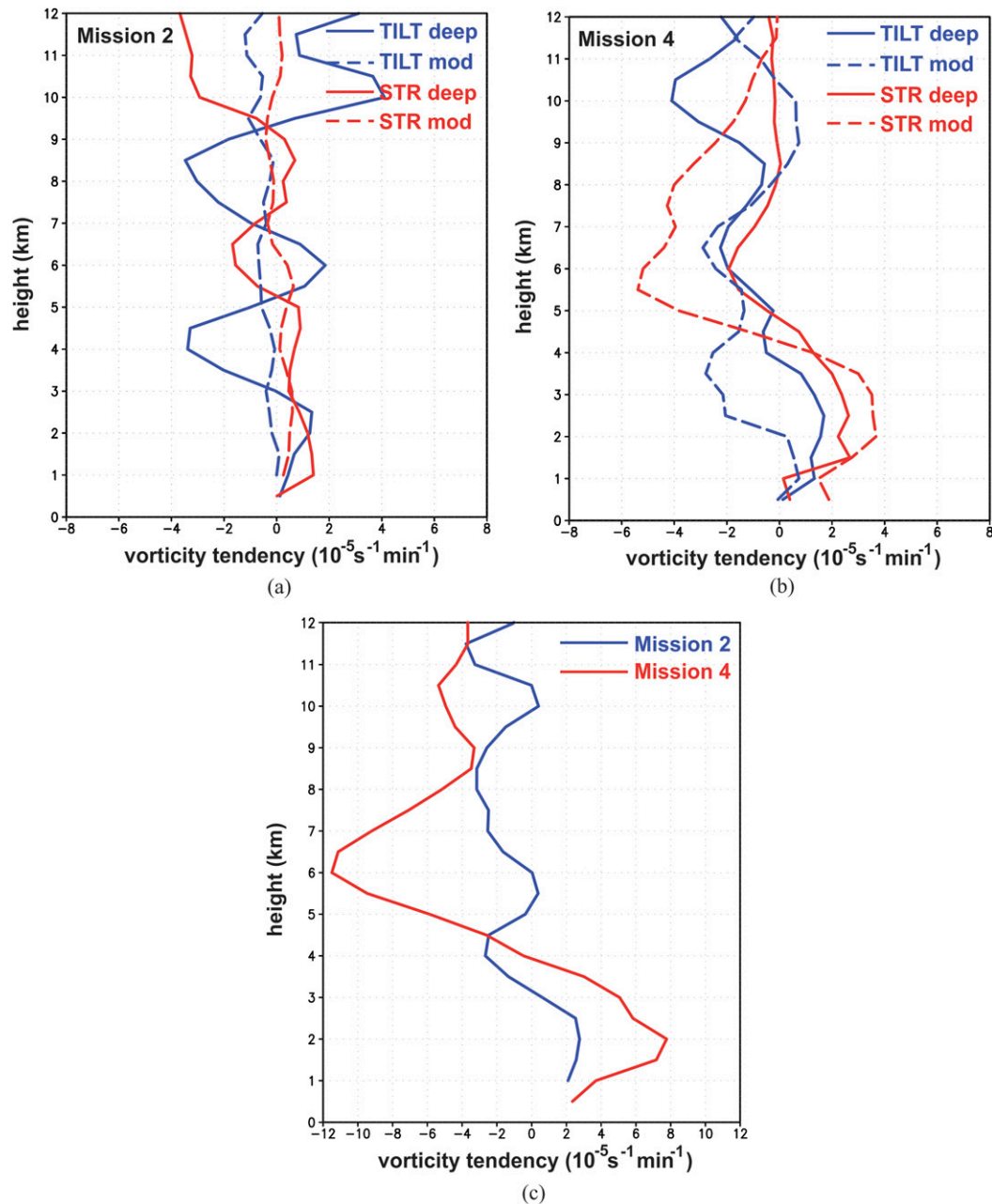


FIG. 17. (a) Profile of average contribution to absolute vorticity tendency ($\times 10^{-5} \text{ s}^{-1} \text{ min}^{-1}$) from tilting (blue) and stretching (red) for regions classified as deep (solid) and moderate (dashed) convection, averaged using three radial passes during mission 2 (160830I1). (b) As in (a), but for three radial passes during mission 4 (160831I1). (c) Sum of averaged contributions from tilting and stretching from deep and moderate convection for mission 2 (blue) and mission 4 (red).

least well removed (i.e., outside the radar domain) from the low-level center for several of the missions into Hermine when it was a tropical depression. This displacement was reflective of the moderate vertical shear Hermine was experiencing, similar to that discussed in [Davis and Ahijevych \(2012\)](#). During mission 4, though, there was a pronounced

midlevel center within ~ 60 km of the low-level center. This proximity was apparent even during the first center pass of this mission. A pass-by-pass analysis during the mission showed that the low-level circulation repositioned to the location of the midlevel circulation, which was also collocated with deep convection downshear.

Such an evolution described above is similar to previous cases of downshear reformation (Molinari et al. 2004, 2006; Molinari and Vollaro 2010; Nguyen and Molinari 2015; Chen et al. 2018). The temporal gap prior to mission 4 precludes a determination of when the midlevel circulation appeared close (i.e., within $\sim 100\text{--}150$ km) to the low-level center. Infrared and microwave satellite imagery during the overnight and early morning hours prior to mission 4, however, showed a broad, persistent area of cold cloud tops with significant ice scattering and liquid water downshear of the low-level center (not shown). The lack of a clear, distinct midlevel circulation within $100\text{--}150$ km of the low-level circulation for several missions prior to mission 4 suggests the development of such a midlevel circulation was tied to episodic periods of convection rather than the sustained presence of a midlevel center near the low-level center. This cannot be determined definitively, though, because of the temporal gap.

2) HOW DID THE STRUCTURE OF PRECIPITATION EVOLVE AND WHAT WAS THE IMPACT OF THIS EVOLUTION ON THE DEVELOPMENT OF HERMINE?

Precipitation, and convection in particular, showed a substantial evolution between missions 2 and 4. Both missions (as well as mission 3), had comparable amounts ($\sim 55\%\text{--}65\%$) of stratiform precipitation. Convection during mission 2 was mostly deep, while during mission 4 convection was primarily of moderate depth. CFADs reflected these transitions in the structure of the dominant convective mode between the two missions. The variation in the depth of the dominant mode of convection between missions 2 and 4 was consistent with changes in the thermodynamic environment toward a more moist and less unstable one as revealed by Global Hawk drops. The air was drier aloft during mission 2, but the greater instability during this mission meant that the dry air likely had a less significant detrimental impact on convection (James and Markowski 2010). While the discussion above implies that changes in the environment drove changes in the structure of the precipitation, it is also quite possible that the precipitation itself modified the local environment in a way that modulated subsequent episodes of precipitation. For example, it has been shown in numerical model simulations (Wang 2014) that shallow and moderate convection (termed cumulus congestus in Wang 2014) can moisten and stabilize the lower and middle troposphere, while deep convection can moisten the upper troposphere. Such a modification to the thermodynamic environment can lead to a greater proportion of moderate convection with a more bottom-heavy mass flux profile.

Deep convection was crucial in amplifying vorticity in the lower troposphere at the location of the midlevel circulation through a combination of stretching and tilting during mission 4. This occurred in the presence of existing higher vorticity and a peak in convergence in the lower troposphere (stretching), as well as pronounced local vertical shear of low-level flow (tilting). On the mesoscale, the circulation was much stronger and deeper in the low- to midtroposphere during mission 4 compared to mission 2. Aggregate vertical mass flux profiles in the mesoscale environment downshear transitioned from a top-heavy profile during mission 2, reflecting the dominance of deep convection in an unstable yet dry environment, to a bottom-heavy profile during mission 4, reflecting the dominance of moderate convection in a moist, relatively stable environment, but also a change in the structure of deep convection. Additionally, the magnitude of the peak aggregate vertical mass flux was much higher during mission 4 than mission 2. This was a result of the much larger coverage of convection ($\sim 28\%$, mostly moderate) during mission 4 compared to the coverage during mission 2 ($\sim 12\%$, mostly deep). Stretching in both moderate and deep convection and tilting in deep convection was maximized in the vorticity-rich environment during mission 4.

Variations in the structure of convection appeared to play a cooperative role across the convective- and mesoscale in facilitating the development of an aligned vortex. On the convective scale, deep convection led to the development of a nearly aligned vortex primarily due to vorticity stretching and tilting, while moderate convection had comparatively less impact on such development. Where the moderate convection had a more substantial impact was on the mesoscale, where the much larger proportion of moderate convection during Mission 4, as well as the change in the structure of the deep convection during this mission, led to a bottom-heavy mass flux profile and a broadscale region of enhanced stretching and tilting in the lower troposphere. In short, deep convection performed the alignment locally, while moderate convection sustained that alignment over a mesoscale spatiotemporal domain. This notion of a multiscale cooperative interaction by convection may be similar to the system-scale spinup driven by VHTs referred to by the Hendricks et al. (2004), Montgomery et al. (2006), Nguyen et al. (2008), and Montgomery and Smith (2014) studies. Relatedly, this interaction is also similar to that described by Wang (2014), who discussed a pathway whereby cumulus congestus (i.e., moderate convection) drives low-level convergence, combining with the rapid development of deep convection in a column moistened by this

congestus to lead to the development of a circulation near the surface.

This multiscale interaction is also consistent with the framework discussed in Tang (2017a), who identified a key metric marking the onset of tropical cyclogenesis as the ratio of bulk differences of moist entropy over differences of angular momentum between an inner and outer region of a developing tropical cyclone. This ratio decreased and became negative in numerical model experiments (Tang 2017b) as both the high-entropy core and low-level vortex in the inner region amplified during tropical cyclogenesis. In the case of Hermine, the ratio would decrease, and likely become negative, as the inner mesoscale domain, incorporating the low-level vortex and immediate environment downshear, moistened (i.e., increased moist entropy), leading to a larger distribution of moderate convection, enhanced lower-tropospheric stretching, and spinup (i.e., increased angular momentum).

Changes in the mass flux profiles between missions 2 and 4, which were linked to changes in the local thermodynamic environment described above, may also have reflected the presence of a midlevel circulation during mission 4 which, from balance considerations (Raymond et al. 2014), would support the presence of a more stable, moister environment. One could imagine a situation where the broad cold cloud shield during the 6–12 h prior to mission 4, mentioned in the previous subsection, reflected the presence of an intense mesoscale convective system that led to the development of a midlevel circulation. The presence of this midlevel circulation would have been reflective of a modified local thermodynamic environment that modulated the structure of the convection and associated mass flux profiles documented in mission 4. But that is speculative at this point.

Differences in the strength of the downdrafts and the amount of weak echoes between missions 2 and 4, also tied to changes in the thermodynamic structure of the environment downshear described above, may have also played a role in the evolution of the low- and midlevel circulations. With more weak echoes and stronger downdrafts during mission 2, there was likely more near-surface divergence and less stretching in the lower troposphere compared with mission 4. This environment may have also prevented the development of moderate convection. Interestingly, the observation of weaker downdrafts during mission 4 was in contrast to the results of Nolan (2007), who noted in his genesis simulations that the frequency of downdrafts was essentially unchanged between a period prior to and at the onset time of genesis, even though the environment came closer to saturated as genesis approached. The reason for this discrepancy is not known at this time, but it is worth exploring further.

Variations in the structure of precipitation showed some indication of being tied to a diurnal cycle, but the cycle was more related to the relative proportion of deep versus moderate convection, rather than convective versus stratiform (as in Bell and Montgomery 2019). Mission 2, during the overnight hours, showed a preponderance of deep convection, while mission 4, during the afternoon, showed a preponderance of moderate convection. Mission 3, which was 24 h prior to mission 4 and also during the afternoon, showed neither deep nor moderate convection, but rather was mostly stratiform and weak echo.

Uncertainties in the vertical velocity retrievals and partitioning algorithm precluded a robust determination from this data what role stratiform precipitation played in Hermine's intensification, even though it has been shown to be an important contributor (Zagrodnik and Jiang 2014; Tao et al. 2017). It is well-known that stratiform precipitation has convergence maximized in midlevels and a top-heavy mass flux profile. Stratiform precipitation identified here, however, showed little variation in its proportion downshear from mission to mission (though there was more stratiform precipitation upshear during mission 4), and mass flux profiles were indeterminate because of uncertainties in the vertical velocity retrievals.

3) WHAT ROLE DID VERTICAL SHEAR PLAY IN HERMINE'S DEVELOPMENT?

Shear is typically considered a negative factor for development of weak TCs because of the potential for advection of dry air above a low-level center, among other reasons. The dry air to the northwest, and upshear, of Hermine's center (cf. Fig. 2) likely played a significant role in preventing deep convection from developing coincident with the low-level center while Hermine was a depression. It is worth noting that there was a substantially higher amount of precipitation upshear during mission 4 compared to mission 2. This may have reflected a vortex that was more aligned during mission 4, as well as possible modifications of the thermodynamic environment upshear.

One beneficial aspect of the persistent northwesterly shear, in this case at least, appeared to be the preconditioning of the mesoscale environment downshear. Repeated cycles of moderate and deep convection associated with mesoscale convective systems downshear may have moistened and stabilized the midlevel and low-level environment, similar to that described in Wang (2014), causing subsequent cycles of convection to have more of a bottom-heavy mass flux profile and maximizing stretching in the lower troposphere. By providing a sustained forcing that focused this preconditioning in a consistent location relative to the low-level circulation, vertical shear may have played a role

similar to the containment role of the wave pouch described in Dunkerton et al. (2009), Montgomery et al. (2010), and Wang (2012). Thus, while vertical shear was initially unfavorable for the intensification of Hermine, its persistence and steady direction and magnitude proved to be a favorable condition for Hermine's eventual alignment and intensification.

b. Future work

There are a variety of ways that the analysis and interpretation of results could be improved. Better vertical velocity retrievals and a more robust partitioning algorithm would allow for an assessment of the role of stratiform precipitation on the vorticity budget, mass flux profile, and development of a persistently aligned vortex during mission 4. Deep-layer thermodynamic observations at a higher temporal resolution than that shown here would provide the ability to better monitor changes in the thermodynamic environment thought to be critical in modulating precipitation mode downshear. Reliable high-resolution numerical model simulations, able to capture the variations in precipitation mode as a function of the local thermodynamic environment, would provide the temporal continuity needed to evaluate the evolution of the low- and midlevel circulation centers as well as calculate robust budgets of vorticity. These efforts will be pursued in an attempt to better characterize and understand the structure and evolution of weak TCs in moderate vertical shear.

Acknowledgments. The authors thank Drs. Xiaomin Chen and Trey Alvey for helpful feedback on the paper. The comments from Dr. Brian Tang and two anonymous reviewers greatly improved the manuscript as well. Finally, we extend our gratitude to the crews of NOAA's Aircraft Operations Center and NASA for their tireless collection of data from the P-3s and GH during this case. This work was supported by NOAA base funds and NASA Grant 80NSSC19K0012 under the direction of Gail Skofronick-Jackson at NASA Headquarters.

REFERENCES

- Alvey, G. R., J. Zawislak, and E. Zipser, 2015: Precipitation properties observed during tropical cyclone intensity change. *Mon. Wea. Rev.*, **143**, 4476–4492, <https://doi.org/10.1175/MWR-D-15-0065.1>.
- , E. Zipser, and J. Zawislak, 2020: How does Hurricane Edouard (2014) evolve toward symmetry before rapid intensification? A high-resolution ensemble study. *J. Atmos. Sci.*, **77**, 1329–1351, <https://doi.org/10.1175/JAS-D-18-0355.1>.
- Bell, M. M., and M. T. Montgomery, 2010: Sheared deep vortical convection in pre-depression Hagupit during TCS08. *Geophys. Res. Lett.*, **37**, L06802, <https://doi.org/10.1029/2009GL042313>.
- , and —, 2019: Mesoscale processes during the genesis of Hurricane Karl (2010). *J. Atmos. Sci.*, **76**, 2235–2255, <https://doi.org/10.1175/JAS-D-18-0161.1>.
- Berg, R., 2016: Tropical Cyclone Report: Hurricane Hermine (28 August–3 September 2016). National Hurricane Center Tropical Cyclone Rep. AL092016, 63 pp, https://www.nhc.noaa.gov/data/tcr/AL092016_Hermine.pdf.
- Bhatia, K. T., and D. S. Nolan, 2013: Relating the skill of tropical cyclone intensity forecasts to the synoptic environment. *Wea. Forecasting*, **28**, 961–980, <https://doi.org/10.1175/WAF-D-12-00110.1>.
- Black, R. A., and J. Hallett, 1986: Observations of the distribution of ice in Hurricanes. *J. Atmos. Sci.*, **43**, 802–822, [https://doi.org/10.1175/1520-0469\(1986\)043<0802:OOTDOI>2.0.CO;2](https://doi.org/10.1175/1520-0469(1986)043<0802:OOTDOI>2.0.CO;2).
- Charney, J. G., and A. Eliassen, 1964: On the growth of the hurricane depression. *J. Atmos. Sci.*, **21**, 68–75, [https://doi.org/10.1175/1520-0469\(1964\)021%3C0068:OTGOTH%3E2.0.CO;2](https://doi.org/10.1175/1520-0469(1964)021%3C0068:OTGOTH%3E2.0.CO;2).
- Chen, X., Y. Wang, J. Fang, and M. Xue, 2018: A numerical study on rapid intensification of Typhoon Vicente (2012) in the South China Sea. Part II: Roles of inner-core processes. *J. Atmos. Sci.*, **75**, 235–255, <https://doi.org/10.1175/JAS-D-17-0129.1>.
- Cram, T. A., M. T. Montgomery, and R. F. Hertenstein, 2002: Early evolution of vertical vorticity in a numerically simulated idealized convective line. *J. Atmos. Sci.*, **59**, 2113–2127, [https://doi.org/10.1175/1520-0469\(2002\)059<2113:EEOVVI>2.0.CO;2](https://doi.org/10.1175/1520-0469(2002)059<2113:EEOVVI>2.0.CO;2).
- Davis, C. A., and D. A. Ahijevych, 2012: Mesoscale structural evolution of three tropical weather systems observed during PREDICT. *J. Atmos. Sci.*, **69**, 1284–1305, <https://doi.org/10.1175/JAS-D-11-0225.1>.
- DeMaria, M., and J. Kaplan, 1999: An updated Statistical Hurricane Intensity Prediction Scheme (SHIPS) for the Atlantic and eastern North Pacific basins. *Wea. Forecasting*, **14**, 326–337, [https://doi.org/10.1175/1520-0434\(1999\)014<0326:AUSHIP>2.0.CO;2](https://doi.org/10.1175/1520-0434(1999)014<0326:AUSHIP>2.0.CO;2).
- Didlake, A. C., and R. A. Houze, 2009: Convective-scale down-drafts in the principal rainband of Hurricane Katrina (2005). *Mon. Wea. Rev.*, **137**, 3269–3293, <https://doi.org/10.1175/2009MWR2827.1>.
- Dunkerton, T. J., M. T. Montgomery, and Z. Wang, 2009: Tropical cyclogenesis in a tropical wave critical layer: Easterly waves. *Atmos. Chem. Phys.*, **9**, 5587–5646, <https://doi.org/10.5194/acp-9-5587-2009>.
- Emanuel, K., C. DesAutels, C. Holloway, and R. Korty, 2004: Environmental control of tropical cyclone intensity. *J. Atmos. Sci.*, **61**, 843–858, [https://doi.org/10.1175/1520-0469\(2004\)061<0843:ECOTCI>2.0.CO;2](https://doi.org/10.1175/1520-0469(2004)061<0843:ECOTCI>2.0.CO;2).
- Fang, J., and F. Zhang, 2010: Initial development and genesis of Hurricane Dolly (2008). *J. Atmos. Sci.*, **67**, 655–672, <https://doi.org/10.1175/2009JAS3115.1>.
- Finocchio, P. M., and S. J. Majumdar, 2017: A statistical perspective on wind profiles and vertical wind shear in tropical cyclone environments of the Northern Hemisphere. *Mon. Wea. Rev.*, **145**, 361–378, <https://doi.org/10.1175/MWR-D-16-0221.1>.
- Fritz, C., Z. Wang, S. W. Nesbitt, and T. J. Dunkerton, 2016: Vertical structure and contribution of different types of precipitation during Atlantic tropical cyclone formation as revealed by TRMM PR. *Geophys. Res. Lett.*, **43**, 894–901, <https://doi.org/10.1002/2015GL067122>.
- Gamache, J. F., 1997: Evaluation of a fully three-dimensional variational Doppler analysis technique. Preprints, 28th Conf. on Radar Meteorology, Austin, TX, Amer. Meteor. Soc., 422–423.
- Gjorgjievska, S., and D. J. Raymond, 2014: Interaction between dynamics and thermodynamics during tropical cyclogenesis. *Atmos. Chem. Phys.*, **14**, 3065–3082, <https://doi.org/10.5194/acp-14-3065-2014>.

- Hence, D. A., and R. A. Houze, 2008: Kinematic structure of convective-scale elements in the rainbands of Hurricanes Katrina and Rita (2005). *J. Geophys. Res.*, **113**, D15108, <https://doi.org/10.1029/2007JD009429>.
- Hendricks, E. A., M. T. Montgomery, and C. A. Davis, 2004: The role of “vortical” hot towers in the formation of Tropical Cyclone Diana (1984). *J. Atmos. Sci.*, **61**, 1209–1232, [https://doi.org/10.1175/1520-0469\(2004\)061<1209:TROVHT>2.0.CO;2](https://doi.org/10.1175/1520-0469(2004)061<1209:TROVHT>2.0.CO;2).
- Heysfield, G. M., J. B. Halverson, J. Simpson, L. Tian, and T. P. Bui, 2001: ER-2 Doppler radar investigations of the eyewall of Hurricane Bonnie during the Convection and Moisture Experiment-3. *J. Appl. Meteor.*, **40**, 1310–1330, [https://doi.org/10.1175/1520-0450\(2001\)040<1310:EDRIOT>2.0.CO;2](https://doi.org/10.1175/1520-0450(2001)040<1310:EDRIOT>2.0.CO;2).
- Holton, J. R., 2004: *An Introduction to Dynamic Meteorology*. 4th ed. International Geophysics Series, Vol. 88, Academic Press, 535 pp.
- Houze, R. A., W. Lee, and M. M. Bell, 2009: Convective contribution to the genesis of Hurricane Ophelia (2005). *Mon. Wea. Rev.*, **137**, 2778–2800, <https://doi.org/10.1175/2009MWR2727.1>.
- James, R. P., and P. M. Markowski, 2010: A numerical investigation of the effects of dry air aloft on deep convection. *Mon. Wea. Rev.*, **138**, 140–161, <https://doi.org/10.1175/2009MWR3018.1>.
- Jiang, H., 2012: The relationship between tropical cyclone intensity change and the strength of inner-core convection. *Mon. Wea. Rev.*, **140**, 1164–1176, <https://doi.org/10.1175/MWR-D-11-00134.1>.
- Jones, S. C., 1995: The evolution of vortices in vertical shear. I: Initially barotropic vortices. *Quart. J. Roy. Meteor. Soc.*, **121**, 821–851, <https://doi.org/10.1002/qj.49712152406>.
- Kilroy, G., and R. K. Smith, 2012: A numerical study of rotating convection during tropical cyclogenesis. *Quart. J. Roy. Meteor. Soc.*, **139**, 1255–1269, <https://doi.org/10.1002/qj.2022>.
- Leighton, H., S. Gopalakrishnan, J. A. Zhang, R. F. Rogers, Z. Zhang, and V. Tallapragada, 2018: Azimuthal distribution of deep convection, environmental factors, and tropical cyclone rapid intensification: A perspective from HWRP ensemble forecasts of Hurricane Edouard (2014). *J. Atmos. Sci.*, **75**, 275–295, <https://doi.org/10.1175/JAS-D-17-0171.1>.
- Leppert, K. D., and D. J. Cecil, 2016: Tropical cyclone diurnal cycle as observed by TRMM. *Mon. Wea. Rev.*, **144**, 2793–2808, <https://doi.org/10.1175/MWR-D-15-0358.1>.
- Marks, F. D., R. A. Houze, and J. F. Gamache, 1992: Dual-aircraft investigation of the inner core of Hurricane Norbert. Part I: Kinematic structure. *J. Atmos. Sci.*, **49**, 919–942, [https://doi.org/10.1175/1520-0469\(1992\)049<0919:DAIOTI>2.0.CO;2](https://doi.org/10.1175/1520-0469(1992)049<0919:DAIOTI>2.0.CO;2).
- Miyamoto, Y., and D. S. Nolan, 2018: Structural changes preceding rapid intensification in tropical cyclones as shown in a large ensemble of idealized simulations. *J. Atmos. Sci.*, **75**, 555–569, <https://doi.org/10.1175/JAS-D-17-0177.1>.
- Molinari, J., and D. Vollaro, 2010: Rapid intensification of a sheared tropical storm. *Mon. Wea. Rev.*, **138**, 3869–3885, <https://doi.org/10.1175/2010MWR3378.1>.
- , —, and K. L. Corbosiero, 2004: Tropical cyclone formation in a sheared environment: A case study. *J. Atmos. Sci.*, **61**, 2493–2509, <https://doi.org/10.1175/JAS3291.1>.
- , P. Dodge, D. Vollaro, K. L. Corbosiero, and F. Marks, 2006: Mesoscale aspects of the downshear reformation of a tropical cyclone. *J. Atmos. Sci.*, **63**, 341–354, <https://doi.org/10.1175/JAS3591.1>.
- Montgomery, M. T., and R. K. Smith, 2014: Paradigms for tropical cyclone intensification. *Aust. Meteor. Oceanogr. J.*, **64**, 37–66, <https://doi.org/10.22499/2.6401.005>.
- , M. Nicholls, T. Cram, and A. Saunders, 2006: A “vortical” hot tower route to tropical cyclogenesis. *J. Atmos. Sci.*, **63**, 355–386, <https://doi.org/10.1175/JAS3604.1>.
- , L. L. Lussier III, R. W. Moore, and Z. Wang, 2010: The genesis of Typhoon Nuri as observed during the Tropical Cyclone Structure 2008 (TCS-08) field experiment—Part I: The role of the easterly wave critical layer. *Atmos. Chem. Phys.*, **10**, 9879–9900, <https://doi.org/10.5194/acp-10-9879-2010>.
- Munsell, E., F. Zhang, J. Sippel, S. Braun, and Y. Weng, 2017: Dynamics and predictability of the intensification of Hurricane Edouard (2014). *J. Atmos. Sci.*, **74**, 573–595, <https://doi.org/10.1175/JAS-D-16-0018.1>.
- Nguyen, L. T., and J. Molinari, 2012: Rapid intensification of a sheared, fast-moving hurricane over the Gulf Stream. *Mon. Wea. Rev.*, **140**, 3361–3378, <https://doi.org/10.1175/MWR-D-11-00293.1>.
- , and —, 2015: Simulation of the downshear reformation of a tropical cyclone. *J. Atmos. Sci.*, **72**, 4529–4551, <https://doi.org/10.1175/JAS-D-15-0036.1>.
- , R. F. Rogers, and P. D. Reasor, 2017: Thermodynamic and kinematic influences on precipitation symmetry in sheared tropical cyclones: Bertha and Cristobal (2014). *Mon. Wea. Rev.*, **145**, 4423–4446, <https://doi.org/10.1175/MWR-D-17-0073.1>.
- , —, J. A. Zawislak, and J. A. Zhang, 2019: Assessing the influence of convective downdrafts and surface enthalpy fluxes on tropical cyclone intensity change in moderate vertical wind shear. *Mon. Wea. Rev.*, **147**, 3519–3534, <https://doi.org/10.1175/MWR-D-18-0461.1>.
- Nguyen, S. V., R. K. Smith, and M. T. Montgomery, 2008: Tropical cyclone intensification and predictability in three dimensions. *Quart. J. Roy. Meteor. Soc.*, **134**, 563–582, <https://doi.org/10.1002/qj.235>.
- Nolan, D. S., 2007: What is the trigger for tropical cyclogenesis? *Aust. Meteor. Mag.*, **56**, 241–266.
- NTSB, 2017: Tropical cyclone information for mariners. MSR-17/02, National Transportation Safety Board, 21 pp.
- Ooyama, K., 1964: A dynamical model for the study of tropical cyclone development. *Geofis. Int.*, **4**, 187–198.
- , 1969: Numerical simulation of the life cycle of tropical cyclones. *J. Atmos. Sci.*, **26**, 3–40, [https://doi.org/10.1175/1520-0469\(1969\)026<0003:NSOTLC>2.0.CO;2](https://doi.org/10.1175/1520-0469(1969)026<0003:NSOTLC>2.0.CO;2).
- , 1982: Conceptual evolution of the theory and modeling of the tropical cyclone. *J. Meteor. Soc. Japan*, **60**, 369–380, https://doi.org/10.2151/jmsj1965.60.1_369.
- Raymond, D. J., and C. López Carrillo, 2011: The vorticity budget of developing Typhoon Nuri (2008). *Atmos. Chem. Phys.*, **11**, 147–163, <https://doi.org/10.5194/acp-11-147-2011>.
- , S. L. Sessions, and C. Lopez Carrillo, 2011: Thermodynamics of tropical cyclogenesis in the northwest Pacific. *J. Geophys. Res.*, **116**, D18101, <https://doi.org/10.1029/2011JD015624>.
- , S. Gjorgjievska, S. Sessions, and Z. Fuchs, 2014: Tropical cyclogenesis and mid-level vorticity. *Aust. Meteor. Oceanogr. J.*, **64**, 11–25, <https://doi.org/10.22499/2.6401.003>.
- Reasor, P. D., and M. D. Eastin, 2012: Rapidly intensifying Hurricane Guillermo (1997). Part II: Resilience in shear. *Mon. Wea. Rev.*, **140**, 425–444, <https://doi.org/10.1175/MWR-D-11-00080.1>.
- , —, and J. F. Gamache, 2009: Rapidly intensifying Hurricane Guillermo (1997). Part I: Low-wavenumber structure and evolution. *Mon. Wea. Rev.*, **137**, 603–631, <https://doi.org/10.1175/2008MWR2487.1>.
- , R. F. Rogers, and S. Lorsolo, 2013: Environmental flow impacts on tropical cyclone structure diagnosed from airborne Doppler radar composites. *Mon. Wea. Rev.*, **141**, 2949–2969, <https://doi.org/10.1175/MWR-D-12-00334.1>.
- Riehl, H., and J. S. Malkus, 1961: Some aspects of Hurricane Daisy. *Tellus*, **13**, 181–213, <https://doi.org/10.3402/tellusa.v13i2.9495>.
- Riemer, M., M. T. Montgomery, and M. E. Nicholls, 2010: A new paradigm for intensity modification of tropical cyclones:

- Thermodynamic impact of vertical wind shear on the inflow layer. *Atmos. Chem. Phys.*, **10**, 3163–3188, <https://doi.org/10.5194/acp-10-3163-2010>.
- Rios-Berrios, R., C. A. Davis, and R. D. Torn, 2018: A hypothesis for the intensification of tropical cyclones under moderate vertical wind shear. *J. Atmos. Sci.*, **75**, 4149–4173, <https://doi.org/10.1175/JAS-D-18-0070.1>.
- Rogers, R. F., 2010: Convective-scale structure and evolution during a high-resolution simulation of tropical cyclone rapid intensification. *J. Atmos. Sci.*, **67**, 44–70, <https://doi.org/10.1175/2009JAS3122.1>.
- , and Coauthors, 2006: The Intensity Forecasting Experiment: A NOAA multiyear field program for improving tropical cyclone intensity forecasts. *Bull. Amer. Meteor. Soc.*, **87**, 1523–1538, <https://doi.org/10.1175/BAMS-87-11-1523>.
- , M. L. Black, S. S. Chen, and R. A. Black, 2007: An evaluation of microphysics fields from mesoscale model simulations of tropical cyclones. Part I: Comparisons with observations. *J. Atmos. Sci.*, **64**, 1811–1834, <https://doi.org/10.1175/JAS3932.1>.
- , S. Lorsolo, P. D. Reasor, J. Gamache, and F. D. Marks Jr., 2012: Multiscale analysis of tropical cyclone kinematic structure from airborne Doppler radar composites. *Mon. Wea. Rev.*, **140**, 77–99, <https://doi.org/10.1175/MWR-D-10-05075.1>.
- , P. D. Reasor, and S. Lorsolo, 2013: Airborne Doppler observations of the inner-core structural differences between intensifying and steady-state tropical cyclones. *Mon. Wea. Rev.*, **141**, 2970–2991, <https://doi.org/10.1175/MWR-D-12-00357.1>.
- , —, and J. Zhang, 2015: Multiscale structure and evolution of Hurricane Earl (2010) during rapid intensification. *Mon. Wea. Rev.*, **143**, 536–562, <https://doi.org/10.1175/MWR-D-14-00175.1>.
- , J. Zhang, J. Zawislak, H. Jiang, G. R. Alvey III, E. J. Zipser, and S. N. Stevenson, 2016: Observations of the structure and evolution of Hurricane Edouard (2014) during intensity change. Part II: Kinematic structure and the distribution of deep convection. *Mon. Wea. Rev.*, **144**, 3355–3376, <https://doi.org/10.1175/MWR-D-16-0017.1>.
- Rygliecki, D. R., J. D. Doyle, Y. Jin, D. Hodyss, and J. H. Cossuth, 2018: The unexpected rapid intensification of tropical cyclones in moderate vertical wind shear. Part II: Vortex tilt. *Mon. Wea. Rev.*, **146**, 3801–3825, <https://doi.org/10.1175/MWR-D-18-0021.1>.
- Smith, R. K., M. T. Montgomery, and S. V. Nguyen, 2009: Tropical cyclone spin up revisited. *Quart. J. Roy. Meteor. Soc.*, **135**, 1321–1335, <https://doi.org/10.1002/qj.428>.
- Steiner, M., R. A. Houze, and S. E. Yuter, 1995: Climatological characterization of three-dimensional storm structure from operational radar and rain gauge data. *J. Appl. Meteor.*, **34**, 1978–2007, [https://doi.org/10.1175/1520-0450\(1995\)034<1978:CCOTDS>2.0.CO;2](https://doi.org/10.1175/1520-0450(1995)034<1978:CCOTDS>2.0.CO;2).
- Stevenson, S. N., K. L. Corbosiero, and J. Molinari, 2014: The convective evolution and rapid intensification of Hurricane Earl (2010). *Mon. Wea. Rev.*, **142**, 4364–4380, <https://doi.org/10.1175/MWR-D-14-00078.1>.
- Susca-Lopata, G., J. Zawislak, E. J. Zipser, and R. F. Rogers, 2015: The role of observed environmental conditions and precipitation evolution in the rapid intensification of Hurricane Earl (2010). *Mon. Wea. Rev.*, **143**, 2207–2223, <https://doi.org/10.1175/MWR-D-14-00283.1>.
- Tang, B., 2017a: Coupled dynamic–thermodynamic forcings during tropical cyclogenesis. Part I: Diagnostic framework. *J. Atmos. Sci.*, **74**, 2269–2278, <https://doi.org/10.1175/JAS-D-17-0048.1>.
- , 2017b: Coupled dynamic–thermodynamic forcings during tropical cyclogenesis. Part II: Axisymmetric experiments. *J. Atmos. Sci.*, **74**, 2279–2291, <https://doi.org/10.1175/JAS-D-17-0049.1>.
- , and K. Emanuel, 2010: Midlevel ventilation’s constraint on tropical cyclone intensity. *J. Atmos. Sci.*, **67**, 1817–1830, <https://doi.org/10.1175/2010JAS3318.1>.
- Tao, C., and H. Jiang, 2015: Distributions of shallow to very deep precipitation–convection in rapidly intensifying tropical cyclones. *J. Climate*, **28**, 8791–8824, <https://doi.org/10.1175/JCLI-D-14-00448.1>.
- , —, and J. Zawislak, 2017: The relative importance of stratiform and convective rainfall in rapidly intensifying tropical cyclones. *Mon. Wea. Rev.*, **145**, 795–809, <https://doi.org/10.1175/MWR-D-16-0316.1>.
- Tao, D., and F. Zhang, 2015: Effects of vertical wind shear on the predictability of tropical cyclones: Practical versus intrinsic limit. *J. Adv. Model. Earth Syst.*, **7**, 1534–1553, <https://doi.org/10.1002/2015MS000474>.
- Wadler, J. B., R. F. Rogers, and P. D. Reasor, 2018: The relationship between spatial variations in the structure of convective bursts and tropical cyclone intensification as determined by airborne Doppler radar. *Mon. Wea. Rev.*, **146**, 761–780, <https://doi.org/10.1175/MWR-D-17-0213.1>.
- Wang, Z., 2012: Thermodynamic aspects of tropical cyclone formation. *J. Atmos. Sci.*, **69**, 2433–2451, <https://doi.org/10.1175/JAS-D-11-0298.1>.
- , 2014: Role of cumulus congestus in tropical cyclone formation in a high-resolution numerical model simulation. *J. Atmos. Sci.*, **71**, 1681–1700, <https://doi.org/10.1175/JAS-D-13-0257.1>.
- , M. T. Montgomery, and T. J. Dunkerton, 2010a: Genesis of pre-Hurricane Felix (2007). Part I: The role of the easterly wave critical layer. *J. Atmos. Sci.*, **67**, 1711–1729, <https://doi.org/10.1175/2009JAS3420.1>.
- , —, and —, 2010b: Genesis of pre-Hurricane Felix (2007). Part II: Warm core formation, precipitation evolution, and predictability. *J. Atmos. Sci.*, **67**, 1730–1744, <https://doi.org/10.1175/2010JAS3435.1>.
- , —, and C. Fritz, 2012: A first look at the structure of the wave pouch during the 2009 PREDICT-GRIP dry runs over the Atlantic. *Mon. Wea. Rev.*, **140**, 1144–1163, <https://doi.org/10.1175/MWR-D-10-05063.1>.
- Wick, G. A., and Coauthors, 2020: NOAA’s Sensing Hazards with Operational Unmanned Technology (SHOUT) Experiment: Observations and forecast impacts. *Bull. Amer. Meteor. Soc.*, <https://doi.org/10.1175/BAMS-D-18-0257.1>, in press.
- Willoughby, H. E., and M. B. Chelmsow, 1982: Objective determination of Hurricane tracks from aircraft observations. *Mon. Wea. Rev.*, **110**, 1298–1305, [https://doi.org/10.1175/1520-0493\(1982\)110<1298:ODOHTF>2.0.CO;2](https://doi.org/10.1175/1520-0493(1982)110<1298:ODOHTF>2.0.CO;2).
- Yuter, S. E., and R. A. Houze, 1995: Three-dimensional kinematic and microphysical evolution of Florida cumulonimbus. Part II: Frequency distributions of vertical velocity, reflectivity, and differential reflectivity. *Mon. Wea. Rev.*, **123**, 1941–1963, [https://doi.org/10.1175/1520-0493\(1995\)123<1941:TDKAME>2.0.CO;2](https://doi.org/10.1175/1520-0493(1995)123<1941:TDKAME>2.0.CO;2).
- Zagrodnik, J. P., and H. Jiang, 2014: Rainfall, convection, and latent heating distributions in rapidly intensifying tropical cyclones. *J. Atmos. Sci.*, **71**, 2789–2809, <https://doi.org/10.1175/JAS-D-13-0314.1>.
- Zawislak, J., H. Jiang, G. R. Alvey III, E. J. Zipser, R. F. Rogers, J. A. Zhang, and S. N. Stevenson, 2016: Observations of the structure and evolution of Hurricane Edouard (2014) during intensity change. Part I: Relationship between the thermodynamic structure and precipitation. *Mon. Wea. Rev.*, **144**, 3333–3354, <https://doi.org/10.1175/MWR-D-16-0018.1>.